Redox state of the South Mountain Batholith: A reconnaissance study using zircon geochemistry

Juan Chavez Cabrera

Department of Earth Sciences
Halifax, Nova Scotia
Canada B3H 4R2
(902) 494-2358

DATE: 28 April 2017

AUTHOR: Juan Chavez Cabrera

TITLE: Redox state of the South Mountain Batholith: A reconnaissance study using zircon geochemistry

Degree: B. Sc. Honours Earth Sciences   Convocation: May   Year: 2019

Permission is herewith granted to Dalhousie University to circulate and to have copied for non-commercial purposes, at its discretion, the above title upon the request of individuals or institutions.

_____
Signature of Author

Distribution License

DalSpace requires agreement to this non-exclusive distribution license before your item can appear on DalSpace.

NON-EXCLUSIVE DISTRIBUTION LICENSE

You (the author(s) or copyright owner) grant to Dalhousie University the non-exclusive right to reproduce and distribute your submission worldwide in any medium.

You agree that Dalhousie University may, without changing the content, reformat the submission for the purpose of preservation.

You also agree that Dalhousie University may keep more than one copy of this submission for purposes of security, back-up and preservation.

You agree that the submission is your original work, and that you have the right to grant the rights contained in this license. You also agree that your submission does not, to the best of your knowledge, infringe upon anyone's copyright.

If the submission contains material for which you do not hold copyright, you agree that you have obtained the unrestricted permission of the copyright owner to grant Dalhousie University the rights required by this license, and that such third-party owned material is clearly identified and acknowledged within the text or content of the submission.

If the submission is based upon work that has been sponsored or supported by an agency or organization other than Dalhousie University, you assert that you have fulfilled any right of review or other obligations required by such contract or agreement.

Dalhousie University will clearly identify your name(s) as the author(s) or owner(s) of the submission, and will not make any alteration to the content of the files that you have submitted.

If you have questions regarding this license please contact the repository manager at dalspace@dal.ca.

Grant the distribution license by signing and dating below.

_____   _____

Name of signatory   Date

Table of Contents

Table of Figures

Table of Tables

Table of Equations

Abstract

The late Devonian South Mountain Batholith (SMB) of Southwestern Nova Scotia is the largest plutonic igneous body emplaced during the Appalachian orogeny, with a current surface expression of 73,000 km^2. The batholith is composed of 13 distinct plutons that are broadly peraluminous in composition, ranging from tonalite to syenogranite. A parameter that has been particularly difficult to quantify for the SMB is the redox state, as measured by the oxygen fugacity (fO_2), which exerts a profound control on magmatic phase stability, element partitioning, and importantly, the potential for economic mineral deposits. We are attempting a redox state survey of mineralised and unmineralised phases of the SMB using the newly-calibrated Ce-in-zircon oxygen barometer. This method combines bulk rock and zircon compositions to calculate apparent zircon/melt partition coefficients for Ce, a parameter which varies with the Ce^{4+}/Ce^{3+} in the melt, and hence oxygen fugacity. A total of 23 samples were collected, of which 13 were selected for zircon separation lithogeochemical analysis based on spatial distribution, mineralogy and preliminary geochemical data acquired with XRF.

Zircons from the unmineralised Halifax and Sandy Lake plutons, and mineralised New Ross plutons were imaged using Cathodoluminescence to determine textural domains, which were a guide to subsequent analysis by electron microprobe and LA-ICPMS. Preliminary examination of REE patterns revealed two distinct groups of zircons in the SMB. The first pattern depicts a continuous increase in REE concentration with increase in ionic radius (La to Lu), large positive Ce anomaly and negative Eu anomaly; these characteristics are typically associated with magmatic zircons. The second pattern also shows a negative Eu anomaly, but a subtler increase in REE concentration from La to Lu and a lack of Ce anomaly; these characteristics are typically associated with hydrothermal zircons. Oxygen fugacity calculations using zircons that exhibit magmatic REE patterns yield four main observations. First, the fO_2 recorded by the SMB shows an apparent internal variation of 4 orders of magnitude. Second, the margin of the Halifax pluton is more reduced than the interior. Third, the mineralised New Ross pluton appears to be the most reduced phase of the sampled phases. Finally, for the SMB, the concentration of dissolved water in the melt imparts a stronger control on redox state than temperature.

Keywords: oxygen fugacity, redox state, zircon, Ce-in-zircon oxygen barometer, cerium, mineralised granites, South Mountain Batholith, S-type granite.

Acknowledgements

Chapter 1. Introduction

1.1 Redox State in Magmatic Systems

The reduction-oxidation (redox) state of an igneous system is a parameter that, like pressure and temperature, imparts a control on the stability of mineral assemblages. Redox state primarily manifests itself in the presence of phases which incorporate substantial quantities of ferric and ferrous iron (Carmichael & Ghiorso, 1990). The composition and occurrence of ferromagnesian silicates in crystallizing melts is controlled by redox state, which in turn is a response to the prevailing oxygen fugacity (Carmichael & Ghiorso, 1990). Oxygen fugacity is a variable used to describe the "potential for iron to occur in a more oxidized or more reduced state" (Frost, 1991).

The relationship between oxygen fugacity and the concentration of FeO and Fe_2O_3 allows us to estimate the prevailing redox, as described by fO_2, through the Carmichael & Ghiorso, (1990) equation:

$$\ln[X_{Fe2O3}/X_{FeO}] = a \ln fO_2 + b/T + c + \sum X_i d_i$$

Equation 1

In this equation for a glassy lava, X is concentration, T is temperature in Kelvin, and a, b, c and d are experimentally derived constants. This relationship has been the theoretical basis for several techniques that aim to constrain absolute oxygen fugacity of magmas. The coexisting Fe-Ti oxides geobarometer is a technique that takes advantage of the relationship observed by Buddington & Lindsley, (1964) between the ilmenite-hematite and the magnetite-spinel solid solutions. At low oxygen fugacities, ilmenite and spinel form the dominant assemblage (Buddington & Lindsley, 1964). At high oxygen fugacities, hematite and magnetite form the dominant assemblage (Buddington & Lindsley, 1964). Based on this relationship, and by determining the composition of both solid solutions, oxygen fugacity can be derived. Other important methods include: V partitioning, Fe^{3+}/Fe^{2+} in melt, and the cerium-in-zircon oxygen barometer. The latter will be discussed in more detail in section 1.3.

There are several assemblages and minerals that contain redox sensitive elements and are suitable for oxygen barometry. Regardless of the specific method, however, most studies discuss results regarding fO_2 using the difference between the absolute $\log fO_2$ value obtained and a known mineral redox buffer. A mineral redox buffer is a chemical reaction that governs the change in

oxygen fugacity (Frost, 1991). The two most commonly used mineral redox buffers are the Nickel-Nickel Oxide (NNO) and the Fayalite-Magnetite-Quartz (FMQ), with the "Δ" notation indicating the log fO2 of the sample relative to the buffer calculated at the same temperature. The FMQ buffer describes the change from ferrous (2+) to ferric (3+) iron (Frost, 1991). In reduced systems, where ferrous iron is the dominant species, ΔFMQ values are below 0 and fayalite prevails (Frost, 1991). The opposite is true in oxidized systems where magnetite crystallizes and iron is predominantly ferric (Frost, 1991). This study will express fO$_2$ values using the ΔFMQ notation.

1.2 Role of Redox State in Ore-forming Processes

Understanding the redox state of magmatic systems can provide invaluable information about the formation conditions of igneous rocks. An area in which understanding this parameter can prove to be useful is ore genesis studies. Redox state changes can aid in the formation of ore deposits by providing a mechanism for precipitation or accumulation of ore-forming minerals. An important example is the speciation of sulfur in magmatic systems that produce porphyry-style mineralization, as described below.

Ballard et al, (2002) show that speciation of sulfur controls whether chalcophile elements (e.g. copper and gold) will accumulate in a late stage fluid phase or in a sulfide liquid. This is because chalcophile elements partition strongly into the sulfide phase but are generally incompatible with sulfate (Ballard et al, 2002). The speciation of sulfur, and subsequent potential for accumulation of chalcophile elements, is a function of oxygen fugacity. At low oxygen fugacity sulfur is present mostly as sulfide (S^{2-}) and at high oxygen fugacity it is present as sulfate (S^{6+}) (Jugo et al, 2004). Therefore, under oxidizing conditions, chalcophile elements will accumulate in the melt during differentiation, because the sulfur-bearing phase that will crystallize is sulfate (Ballard et al, 2002). Hence, resulting late-stage magmatic fluids will be rich in chalcophile elements and can generate mineralization of economic interest under the right conditions (Ballard et al, 2002).

1.3 Ce-in-zircon Oxygen Barometry

Zircon (ZrSiO$_4$) is a common mineral in intermediate to Si-saturated igneous rocks (Hoskins & Schaltegger, 2003). It is the main host for zirconium (Zr), but also hosts considerable fractions of U, Th, Hf, and REE in relation to whole-rock abundances (Hoskins & Schaltegger, 2003). Zircon has been utilized extensively for U-Th-Pb geochronology as it is refractory and resistant to weathering and isotopic resetting. However, an important feature of zircon has been

underutilized until recently (Smythe & Brenan, 2016); the chondrite-normalized concentration of Ce in zircon is anomalously high relative to adjacent REE (Hoskins & Schaltegger, 2003) and ubiquitous in all terrestrial magmatic zircon (Trail et al, 2012). This anomaly is a result of zircon preferentially accommodating Ce^{4+} (as opposed to Ce^{3+}) into its structure due to the similarities in both charge and ionic radius to Zr^{4+} (Smythe & Brenan, 2016 based on Shannon, 1976).

The cerium-in-zircon oxygen barometer takes advantage of this anomaly to describe the oxygen fugacity of a melt during the crystallization of zircon. This is possible because the speciation of cerium is a function of oxygen fugacity (Smythe & Brenan, 2013). At low oxygen fugacity, cerium exists mostly as Ce^{3+} and at high oxygen fugacity it is found as Ce^{4+} (Smythe and Brenan, 2013). This relationship is recorded in zircons because at high oxygen fugacity, the partition coefficient of cerium in zircon is higher than at low oxygen fugacity (Smythe & Brenan, 2016).
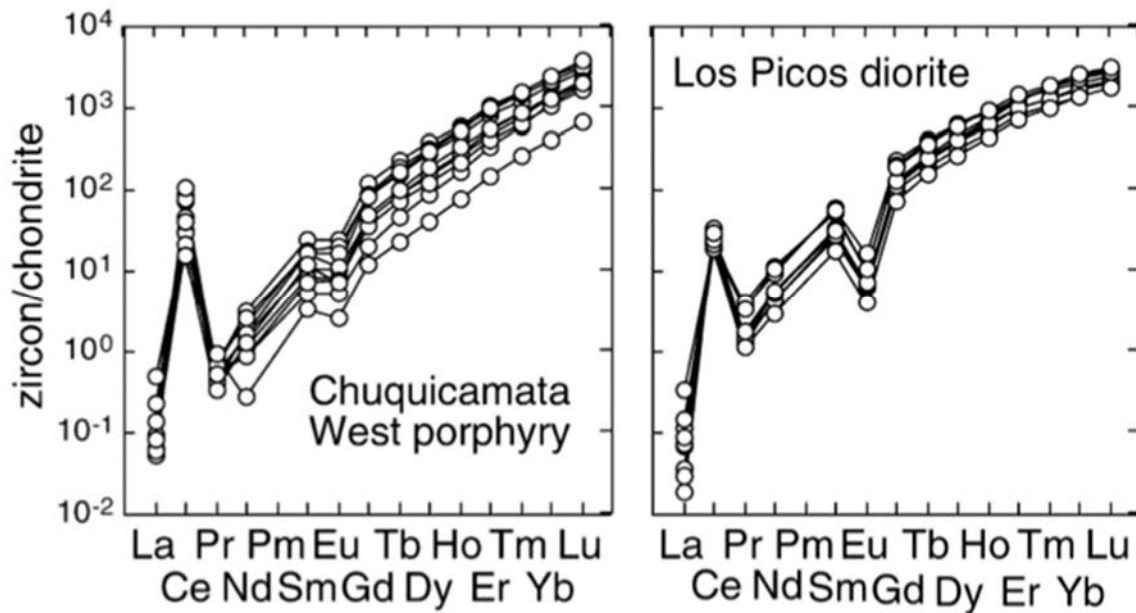
Figure 1 Chondrite-normalized REE plots for the mineralised Chuquicamata West Porphyry and unmineralised Los Picos Diorite of the Chuquicamata – El Abra Belt in Chile (Ballard et al, 2002). Both phases exhibit a strong positive cerium anomaly with different magnitudes. Ballard et al, 2002 use the difference in magnitude to highlight the difference in redox state of both phases.

The technique utilizes the concentration of Ce in zircon and melt, and values for the partition coefficient of cerium (3+ and 4+) between zircon and melt as an equivalence for the mole

fractions of Ce^{4+} and Ce^{3+} in the melt (Smythe & Brenan, 2016). These proportions are then related to melt oxygen fugacity through the Smythe & Brenan, (2016) equation:

$$\ln \frac{X_{Ce^{4+}}^{melt}}{X_{Ce^{3+}}^{melt}} = \frac{1}{4}\ln fO_2 + \frac{13136(\pm591)}{T} - 2.064(\pm0.011)\frac{NBO}{T} - 8.878(\pm0.112) \cdot$$

$$xH_2O - 8.955(\pm0.091)$$

Equation 2

Where X is concentration, T is temperature, and NBO/T is the ratio of non-bridging oxygen atoms per tetrahedral site. T is estimated through the Ferry and Watson, (2007) Ti-in-zircon geothermometer using the activities of silica and rutile. The concentration of dissolved water in the melt can be estimated through inferred temperature and depths, and water concentration relationships described in Baker & Alletti, (2012). Finally, the concentrations of cerium in the melt and zircon are determined by whole-rock and in-situ zircon analysis of samples from the South Mountain Batholith. This barometer is useful in this setting because zircon is ubiquitous in all phases (MacDonald, 2001) and coexisting Fe-Ti oxides are rare (Clarke & Carruzzo, 2007).

1.4 Objective of Study

The objective of this study is to use the newly-calibrated Ce-in-zircon oxygen barometer (Smythe & Brenan, 2016) to conduct a reconnaissance survey of the redox state of mineralised and unmineralised phases of the South Mountain Batholith. Results will help to determine if there is a spatial/temporal relationship between mineralization and redox state across different plutons. Additionally, the survey might help determine if the assimilation of country rock affects the oxygen fugacity within and between plutons.

Chapter 2. Regional Background

2.1 Regional Setting

The province of Nova Scotia is composed of two different tectonic terranes: Avalon and Meguma. The Avalon Terrane, which today lies north of the Cobequid-Chedabucto fault system, was formed at the margin of Gondwana and began rifting away from that continental land-mass during the Late Cambrian- Early Ordovician (Murphy, Hamilton & LeBlanc, 2012). Avalonia migrated north until it became accreted onto Laurentia, marking the closure of the Iapetus Ocean during the Silurian (Murphy, Hamilton & LeBlanc, 2012). The Meguma Terrane had a similar tectonic history, forming along the boundaries of northern Gondwana (Schenk, 1997) and later accreted onto Laurentia during the Devonian (Keen et al, 1991).
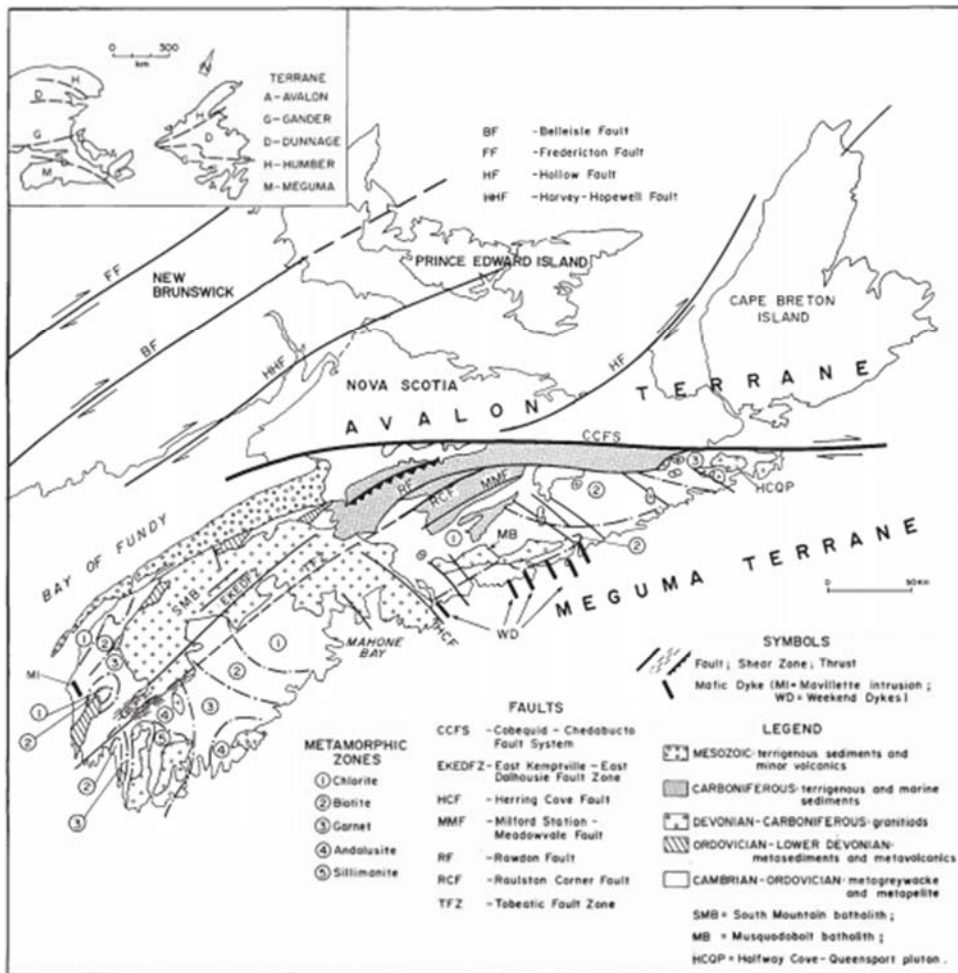
Figure 2 Regional map of Nova Scotia highlighting the major lithotectonic groups of the Meguma Terrane (Horne et al, 1992)

The Meguma terrane was thrust onto the Avalon terrane that had, itself, been only recently accreted onto Laurentia (Keen et al, 1991). It has been argued that granulite facies rocks of the Avalon terrane constitute the basement for the Meguma terrane (Eberz et al, 1991). Furthermore, these high-grade metamorphic basement rocks have been interpreted to have both igneous and sedimentary protoliths based on studies of xenoliths found within the Tangier Dyke of Nova Scotia (Eberz et al, 1991).

As a 'peri-Gondwana' continent, Meguma accumulated large volumes of turbidite fan deposits, interpreted to be part of a tectonically quiescent continental margin depositional environment (Shellnutt and Dostal, 2015 from Schenk, 1997). These turbidites were later metamorphosed under lower greenschist to upper amphibolite facies as a result of compression during the Acadian Orogeny (Shellnutt and Dostal, 2015 from Schenk, 1997). In addition to these metasedimentary packages, the Meguma terrane also hosts a variety of igneous intrusive and volcanic rocks, including the largest   intrusion associated with the Acadian Orogeny, the South Mountain Batholith (SMB).

2.2 Emplacement of the SMB

The SMB is composed of 13 distinct plutons that cover approximately 7,300 km^2 of southwestern Nova Scotia (Horne et al, 1992). The batholith intruded the Meguma Terrane during the late stages of the Devonian-aged Acadian Orogeny and has been dated at 370-380 Ma (Horne et al, 1992). The intrusion post-dates regional deformation based on the truncation of pre-existing, Middle-Devonian NE-trending regional folds associated with the orogeny (Horne et al, 1992). However, the batholith shows internal features such as biotite alignment and megacryst-xenocryst concentrations that are interpreted to reflect the structural controls imposed by regional transpression (Horne et al, 1992). Furthermore, these relationships serve as evidence that the ascent and localization of the SMB is likely related to crustal-scale NE-trending fault systems (Horne et al, 1992). The batholith was formed through two different magma injection periods, which gave way to the distinction between Stage I and Stage II plutons (Horne et al, 1992). Stage I plutons are less evolved bodies (granodiorites to monzogranites) that envelope the more evolved (monzogranites to leucogranites) Stage II plutons (Horne et al, 1992). After ascent of these magmas, stoping served as the final emplacement mechanism (Horne et al, 1992). This is a process that occurs when large, brittle blocks of overlying country rock fall into a rising magma and are sufficiently dense to sink into it (Winter, 2010).
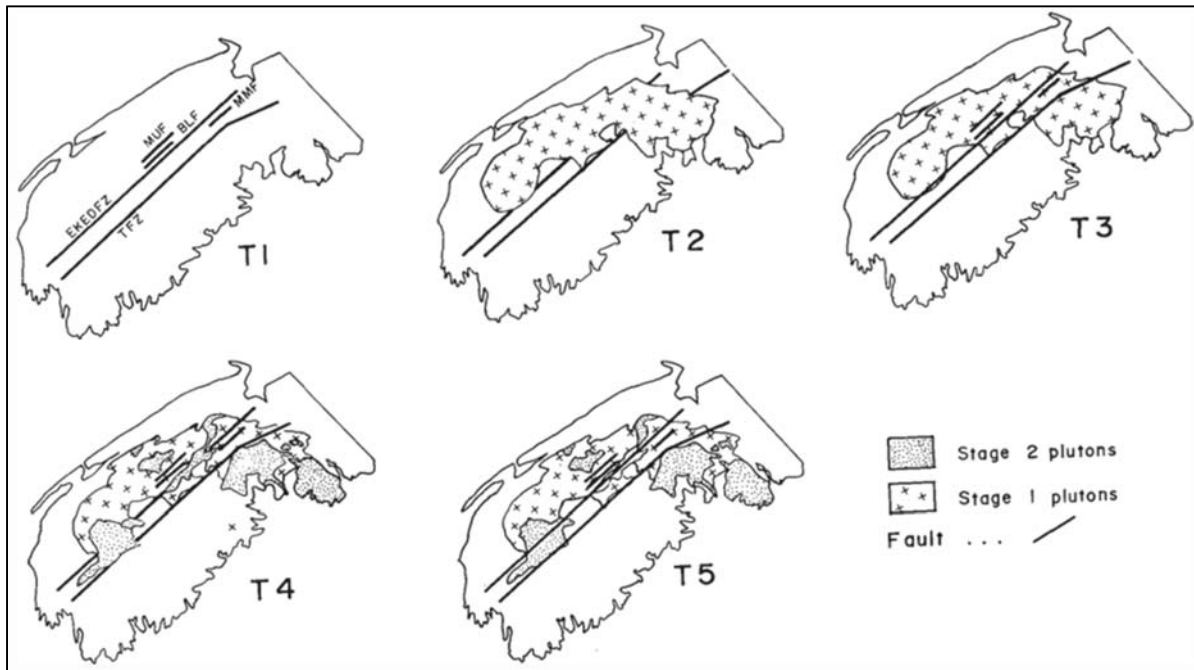
Figure 3 . Summary of the emplacement history of Stage I and Stage II plutons of the SMB and their relationship with pre-existing regional deformation (Horne et al, 1992). (T1) reflects NE-trending regional faulting prior to intrusion. (T2) initial emplacement of Stage I plutons. (T3) reactivation of regional faults, which fracture the emplaced Stage I plutons. (T4) emplacement of Stage II plutons with minor structural control from regional faults. (T5) reactivation of regional faults.

2.3 Mineralogy of the SMB

Previous studies have determined that the mineralogical assemblage of the SMB is consistent with the S-type characteristics proposed by Chappell & White, (1974). Although the modal mineralogy of the SMB varies from pluton to pluton, most of the batholith is composed of monzogranites, with minor components of granodiorites and leucogranites (MacDonald, 2001). The SMB mineralogy is consistent with the expected assemblage of peraluminous granites (Clarke, 1981), which is a distinctive characteristic of S-type granites (Chappell & White, 1974). The batholith contains magmatic quartz + two feldspars + one or more characteristic phases such as biotite, muscovite, cordierite, andalusite and topaz (MacDonald, 2001). An additional line of evidence to characterize the SMB as an S-type granite is the presence of ilmenite (MacDonald, 2001). The distinction between ilmenite-series and magnetite-series granites presented by Sasaki & Ishihara, (1979), although equivocal in some cases, presents a strong division between igneous and sedimentary sources. The distinction also provides some genetic implications – ilmenite-series granites, associated with sedimentary sources, are thought to have source magmas formed at

relatively shallow depths and have undergone possible incorporation of carbon-bearing metamorphic and sedimentary rocks (Sasaki & Ishihara, 1979).

2.4 Geochemistry of the SMB

The bulk rock composition of Stage I and II plutons of the SMB also suggest a sedimentary source. The Shand index, which discriminates between peraluminous, metaluminous and peralkaline suites, was implemented to examine the $Al_2O3/[NaO+CaO+K_2O]$ ratio by MacDonald, (2001). Aside from demonstrating the peraluminosity of the batholith, this ratio also seems to show an increasing order of aluminum saturation with increasing order of differentiation (MacDonald, 2001). More detailed characteristics regarding major element composition of the batholith are discussed in section 4.1.

The trace element composition of the batholith suggests there is zoning in every pluton. Stage I plutons tend to exhibit 'normal' zoning, whereas Stage II seem to exhibit both normal and 'reverse' zoning (MacDonald, 2001). For MacDonald, 2001, normal zoning refers to plutons with less evolved margins and more evolved cores and the opposite is true for reverse zoning (MacDonald, 2001).

Neodymium model ages obtained from metapelitic xenoliths of the Tangier Dyke yield similar ages as the Avalon terrane (Eberz et al, 1991). Additionally, Nd-Sr isotopic compositions of metapelitic xenoliths interpreted to derive from the Avalon terrane make it a suitable protolith for the peraluminous SMB (Eberz et al, 1991). This xenoliths also have high (Th+U), Zr/Hf, and ∑REE relative to the modern mantle, which serves as further evidence of metapelitic source.

2.5 Mineralisation in the SMB

The SMB hosts a wide variety of ore deposits that are primarily found in the more differentiated Stage II plutons and appear to be localized along major fault zones that imply they are structurally controlled (MacDonald, 2001). SMB deposits vary significantly in mineralisation style and ore mineral association. The batholith hosts minor breccia- and peribatholitic-style deposits of economic interest associated with Pb, Zn, Ba, Sn and W (MacDonald, 2001). However, the most important deposits are greisen-, vein-, and pegmatite-style deposits and are best exemplified by the East Kemptville, Millet Brook, and New Ross deposits, respectively (MacDonald, 2001).
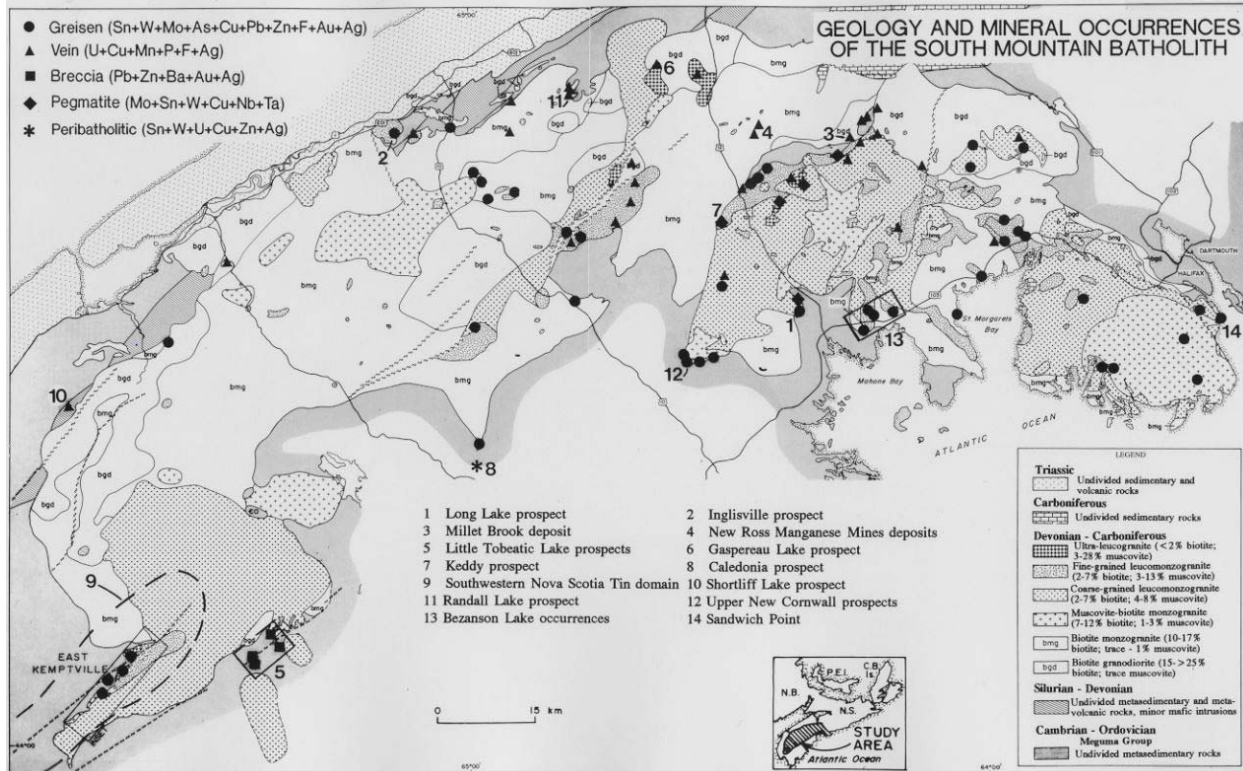
Figure 4 Geologic map of the SMB showing the spatial distribution of greisen, vein, breccia, pegmatite, and peribatholitic deposits found within the intrusion (MacDonald, 2001).

The East Kemptville Sn-Zn-Cu-Ag deposits are hosted in the Davis Lake complex in the westernmost portion of the SMB (Kontak, 1990). More specifically, the deposits are hosted within the East Kemptville topaz-muscovite leucogranite, which is an uncommon assemblage in the SMB due to the presence of topaz (Kontak, 1990). This mineralised magmatic phase occurs within the northeast trending East Kemptville Shear Zone (Kontak, 1990), suggesting that regional structures influence mineralisation in the region. These greisen-style deposits are interpreted to be of magmatic-hydrothermal source based on petrography and trace element distribution (Kontak, 1990). The main economic mineral in these deposits is cassiterite and it is predominantly found disseminated within greisenised leucogranite (Kontak, 1990; MacDonald, 2001).

The Millet Brook U vein-style deposits are hosted in biotite granodiorites and the Salmontail Lake biotite monzogranite of the New Ross and Salmontail plutons (Chatterjee et al, 1982; MacDonald, 2001). The host lithology is composed of quartz, two feldspars, biotite, muscovite, apatite, pyrite, zircon, pyrrhotite and ilmenite (Chatterjee et al, 1982). The deposits have been interpreted to be genetically associated to the structurally controlled leucomonzogranite injections of the area (Chatterjee et al, 1982; MacDonald, 2001). Furthermore, mineralisation

9

appears to be concentrated in en-echelon fractures zones that reflect shearing in the region (MacDonald, 2001 from Chatterjee et al 1985).

Chapter 3. Methodology

Samples were collected across multiple localities exhibiting different phases of the SMB to analyse in-situ zircon. Each sample was divided into 3 pieces to: (a) conduct an XRF analysis and produce thin sections, (b) analyse whole-rock composition, and (c) to obtain zircon pan-concentrates. Zircon crystals from pan-concentrate were selected, mounted and analysed for trace element composition. This process resulted in the whole-rock and zircon geochemical data required to estimate oxygen fugacity values through the cerium-in-zircon oxygen barometer.

3.1 Sampling

Sampling was conducted during June and July of 2018. The first set of samples were obtained from a traverse along NS-306 (Old Sambro Road), which exhibits several outcrops of the differentiated Harrietsfield monzogranite. Thirteen samples were retrieved from these outcrops in order to (a) determine the oxygen fugacity of an unmineralised phase of the SMB and (b) examine if the oxygen fugacity varies systematically with increasing differentiation from the margin to the interior of the intrusion. This set of samples also includes two from the Chain of Lakes trail in Bayers Lake, near the contact between the SMB and Halifax Formation of the Meguma Terrane. These samples were obtained to examine if the assimilation of country rock would have an impact on oxygen fugacity. A set of 7 samples were retrieved from road cuts along NS Highway 103, which transects the Sandy Lake and Panuke Lake plutons. These samples were collected to examine the oxygen fugacity of another unmineralised phase. The final set of samples was retrieved from deposits around the New Ross Area. This includes samples from Keddy, Long Lake and Millet Brook Deposits, which are primarily associated with Mo-Sn, Sn and U mineralisation, respectively. These samples were collected to determine the oxygen fugacity of phases of the SMB that host ore deposits. The following table provides a summary of data acquired during sampling.

Table 1 Summary of field samples collected

Sample #	UTM E	UTM N	Lithology	Pluton
18JC0001	449381	4938638	megacrystic monzogranite	SMB, Halifax
18JC0002A	448992	4936856	megacrystic monzogranite	SMB, Halifax
18JC0002B	448992	4936856	mg leucomonzogranite pod	SMB, Halifax
18JC0002C	448992	4936856	fg leucomonzogranite dyke	SMB, Halifax
18JC0003	449154	4933734	megacrystic monzogranite	SMB, Halifax
18JC0004	449507	4927713	megacrystic monzogranite	SMB, Halifax
18JC0005	450623	4926470	megacrystic monzogranite	SMB, Halifax
18JC0006A	451644	4925428	megacrystic monzogranite	SMB, Halifax
18JC0006B	451644	4925428	fg leucomonzogranite dyke	SMB, Halifax
18JC0007	452474	4924658	megacrystic monzogranite	SMB, Halifax
18JC0008	447604	4943099	megacrystic granodiorite	SMB, Halifax
18JC0009	445996	4943173	megacrystic monzogranite	SMB, Halifax
18JC0010	422977	4948571	megacrystic monzogranite	SMB, Sandy Lake
18JC0011	422878	4948558	mg leucomonzogranite pod	SMB, Sandy Lake
18JC0012	428976	4951313	megacrystic monzogranite	SMB, Sandy Lake
18JC0013	427778	4950823	megacrystic monzogranite	SMB, Sandy Lake
18JC0014	427037	4950221	megacrystic monzogranite	SMB, Sandy Lake
18JC0015	427021	4950211	megacrystic monzogranite	SMB, Sandy Lake
18JC0016	425491	4949579	mg leucomonzogranite pod	SMB, Sandy Lake
18JC0017	431163	4950229	megacrystic monzogranite	SMB, Sandy Lake
18JC0018	433864	4948796	mg leucomonzogranite pod	SMB, Sandy Lake
18JC0019	391494	4939641	greisenized monzogranite	SMB, New Ross
18JC0020	382102	4953231	mg leucomonzogranite pod	SMB, New Ross
18JC0021	399559	4968101	megacrystic monzogranite	SMB, New Ross
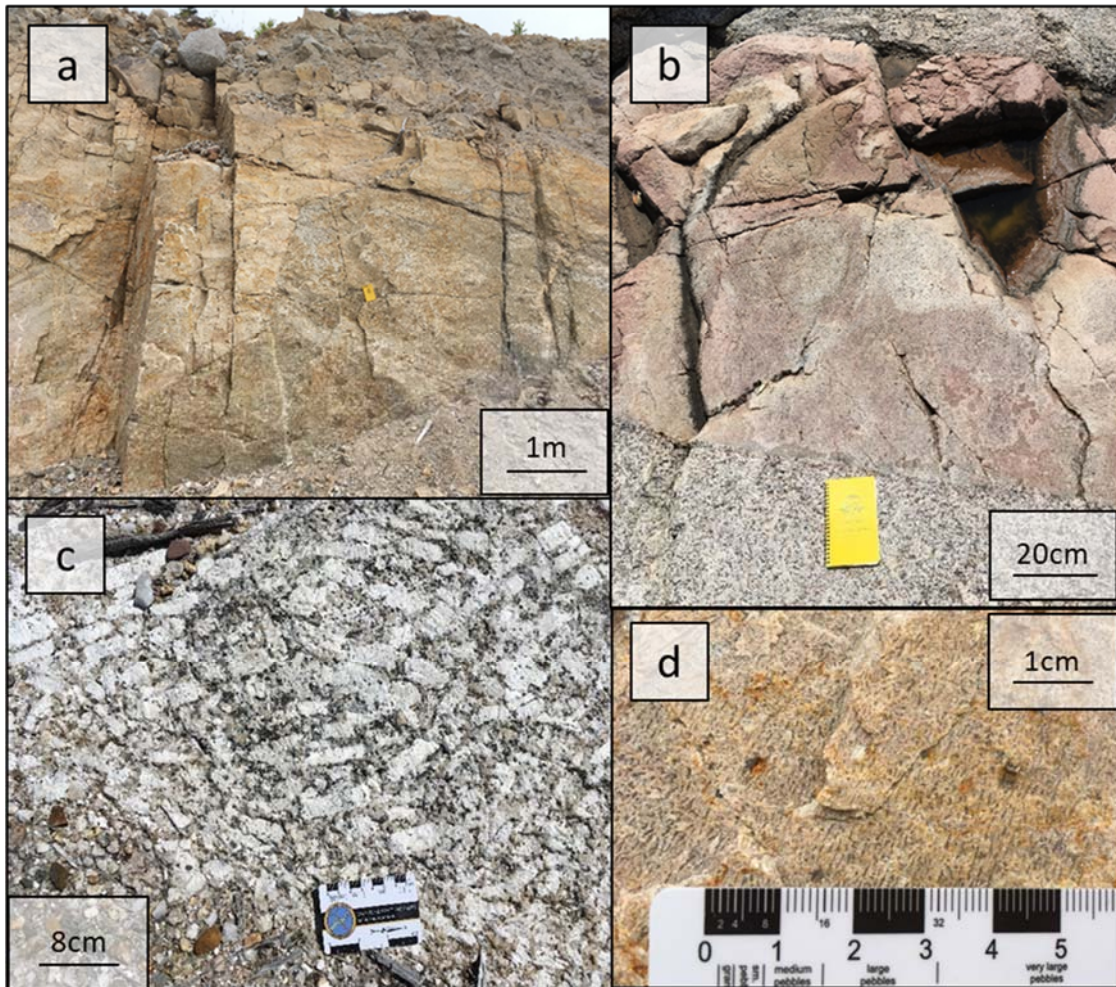
Figure 5 . Examples of structures observed in the field. (a) Two magmatic phases that are possible evidence of magma mixing in Sandy Lake pluton outcrop along NS Highway 103. (b) Aplite dyke cross-cutting a monzogranite from the Halifax Pluton. (c) Concentration of alkali feldspar phenocrysts in the Halifax pluton. (d) Granophyric texture in Sandy Lake pluton.

3.2 Whole-Rock Lithogeochemistry

Whole-rock geochemical data was acquired by Activation Laboratories Ltd. (ACTLABS). Major element composition was determined through Lithium Metaborate/ Tetraborate Fusion – ICP. Trace element composition was determined through Lithium Metaborate/ Tetraborate Fusion – Inductively Coupled Mass Spectrometry (ICPMS).

3.3 Sample Preparation

Mineral separation was performed on kg-sized samples at Overburden Drilling Management Ltd (Ottawa, Canada) using electric pulse disaggregation followed by density

13

separation. Individual zircons were hand-picked from the resulting pan concentrate, which were then annealed in silica crucibles at 900 ℃ for 60 hours to enhance the cathodoluminescence response, according to Nasdala et al. (2002). The resulting crystals were then mounted on double-sided tape, which was then back-filed with epoxy enclosed in 1" diameter rings. The surface of the pucks were then ground with 600 grit silicon carbide paper, then polished in water using 1 µm followed by 0.3 µm alumina powder.

Figure 6 (a) Entire field of view of original pan concentrate from which individual zircons are selected. (b) Utensils used to pick zircon crystals: (1) thin section slide, (2) double sided tape, (3) alumina container for (4) silica crucible, and (5) silica rods with melted ends to pick crystals. (c) 0.3 µm disc for polishing epoxy puck (sitting on disc). (d) Polished puck with sample 18JC0008 zircon under transmitted light microscope.

3.4 Cathodoluminescence (Cl) Imaging

Cl-imaging was performed at the Saint Mary's University Electron Microscopy Centre (EMC). The instrument used was a TESCAN MIRA 3 LMU Variable Pressure Schottky Field Emission Scanning Electron Microscope (SEM), with a maximum resolution of 1.2 nm at 30 kV. The instrument used to acquire the Cl images was a Gatan miniCL imaging system, which is equipped to capture emissions in the 185~850 nm wavelength range. The SEM imaging was essential to place zircon analyses into a textural perspective. Internal zircon structures, such as

zoning or inherited cores, are not readily evident through backscattered electron (BSE) imaging or optical microscopy. The working conditions used to acquire 67 Cl-images and BSE images (for reference) were: 20 kV, 19 nm spot size, and beam current of 15.00 nA.

3.5 Electron Probe Micro-Analyzer (EPMA)

The major element composition of zircon crystals was determined using the JEOL JXA-8200 EPMA in the Robert M. MacKay Electron Microprobe Laboratory at Dalhousie University. Zircon crystal analyses were done using an accelerating voltage of 15 kV, a beam current of 20 nA and an effective spot size of 1 μm. Standards for zircon crystals were: Zircon for Si and Zr, Hafnon for Hf, Apatite for P, and Yttrium-Aluminum Garnet (YAG) for Y. Count times on peak position were 20 seconds, and 10 seconds at each background position. The data reduction scheme used was ZAF.

3.6 Laser Ablation Inductively Coupled Plasma Mass Spectrometry (LA-ICP-MS)

Trace element concentrations of zircons were determined using the LA-ICP-MS facility located in the Health and Environments Research Centre [HERC] Laboratory at Dalhousie University. The system employs a frequency quintupled Nd:YAG laser operating at 213 nm, coupled to a Thermo Scientific iCAP Q ICP-MS quadrupole mass spectrometer with He flushing the ablation cell to enhance sensitivity (Eggins et al. 1998). Individual zircons were analyzed using a laser repetition rate of 10 Hz and a spot size of 25 μm, with laser output adjusted to achieve a beam irradiance of 5 J/cm^2. Factory-supplied time-resolved software was used for the acquisition of individual analyses. A typical analysis involved 20 seconds of background acquisition with the ablation cell being flushed with He, followed by ablation for 60 seconds, then 60 seconds of cell washout. Analyses were collected in a sequence in which 2-4 analyses were done on two standard reference materials (NIST 610 and BIR1) at the start of the acquisition cycle, then after every 13-17 analyses on the unknown samples. At least two analyses were done on each zircon depending on zonation and crystal size. Data reduction was done off-line using the Iolite version 3.6 software package. Ablation yields were corrected by reference to the known concentration of Zr as determined by EPMA.

3.7 Oxygen Fugacity and Temperature Calculations

The cerium-in-zircon oxygen barometer was employed to obtain fO_2 values recorded in analysed zircon. The Microsoft Excel spreadsheet provided in Smythe & Brenan, (2016) requires the user to input: (a) whole rock major element concentration, (b) whole rock REE and U, Th, Hf concentration, (c) zircon REE and U, Th, Hf concentration, (d) activity of SiO_2, (e) activity of TiO_2, and (f) concentration of dissolved H_2O in the melt. Values for (a), (b) and (c) were determined by direct analyses of the samples and the remaining fields were estimated. The justification for the values used will be outlined in the next chapter.

The spreadsheet has two main sheets. The first sheet has the open fields in which values are input and a graph of the distribution coefficient (D) for 3+ and 4+ cations vs. ionic radii. This graph is used as a visual tool to illustrate the deviation from the theoretical expected distribution of 3+ and 4+ cations in zircon. The second sheet outlines the obtained ΔFMQ, log $fO2$, Ce^{4+}/Ce^{3+}_{melt}, D $Ce_{zircon/melt}$, T (K), and NBO/T. It also outlines error values and statistics on the slope of the best fit line for 3+ and 4+ cations.
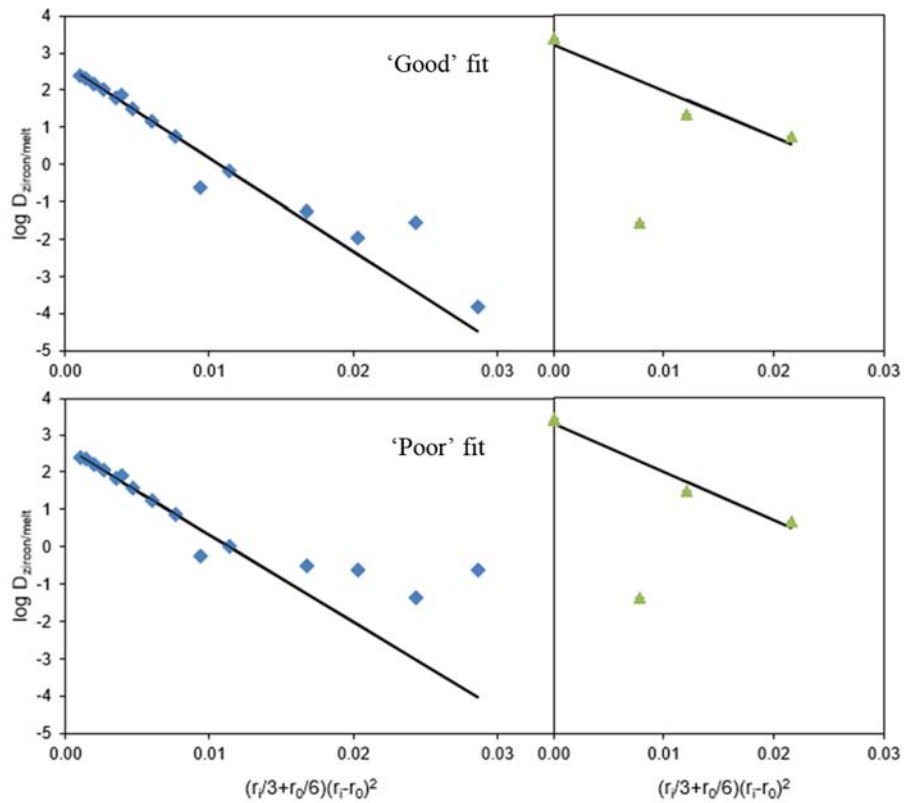
Figure 7 $D_{zircon/melt}$ vs. ionic radii parameter for 3+ (diamond) and 4+ (triangle) obtained for different analyses. A 'Good' fit graph is considered to have minor or no deviation from the expected theoretical trend shown by the solid black line. Analyses that show 'Poor' fits have a considerable deviation from the expected trend, suggestive of processes other than magmatic. Both of these graphs were produced from sample 18JC0021, corresponding to the New Ross pluton; the only difference between these calculations was their zircon trace element concentration.

Areas in yellow require input. Note that the input for H2O will be normalised to 100%.

Parent Melt Composition

	SiO$_2$	TiO$_2$	Al$_2$O$_3$	MgO	MnO	FeO	Fe$_2$O$_3$	CaO	Na$_2$O	K$_2$O	P$_2$O$_5$	H$_2$O	Total
	wt.% (σ)	wt.% (σ)	wt.% (σ)	wt.% (σ)	wt.% (σ)	wt.% (σ)	wt.% (σ)	wt.% (σ)	wt.% (σ)	wt.% (σ)	wt.% (σ)	wt.% (σ)	
18JC 0021	68.38 (0.00)	0.61 (0.00)	14.01 (0.00)	1.14 (0.00)	0.07 (0.00)		4.46 (0.00)	1.58 (0.00)	2.97 (0.00)	4.07 (0.00)	0.22 (0.00)	9.00 (0.00)	106.52

Trace Element Concentration

	Element	Melt ppm (σ)	Zircon ppm (σ)
18JC 0021	Y	31.0 (0.0)	2290 (0.0)
	La	34.3 (0.0)	0.0053 -
	Ce	73.0 (0.0)	2.01 (0.0)
	Pr	8.9 (0.0)	0.098 (0.0)
	Nd	34.8 (0.0)	2.02 (0.0)
	Sm	8.4 (0.0)	5.55 (0.0)
	Eu	1.1 (0.0)	0.268 (0.0)
	Gd	7.2 (0.0)	42.3 (0.0)
	Tb	1.1 (0.0)	15.6 (0.0)
	Dy	6.6 (0.0)	205 (0.0)
	Ho	1.2 (0.0)	72.7 (0.0)
	Er	3.1 (0.0)	335 (0.0)
	Tm	0.4 (0.0)	64.3 (0.0)
	Yb	2.6 (0.0)	556 (0.0)
	Lu	0.4 (0.0)	100.6 (0.0)
	Ti	3674.3 (0.0)	6.08 (0.0)
	Zr	184.0 (0.0)	448000 (0.0)
	Hf	4.5 (0.0)	11250 (0.0)
	Th	12.1 (0.0)	68 (0.0)
	U	14.5 (0.0)	323 (0.0)

σ_{SiO2}	σ_{TiO2}
1.000	0.500

log fO_2		Δ FMQ	
value	error	value	error
-17.24 (1.55)		-1.70 (1.55)	

Figure 8 Snap-shot of Microsoft Excel sheet used to input required fields for fO$_2$ calculations.

18

Chapter 4. Results

4.1 Whole Rock Geochemistry

The following section aims to outline the main geochemical characteristics of all the samples collected and put them into context of previous studies on the SMB. Silica variation, chondrite normalized REE and multi-REE variation diagrams were plotted to illustrate major, minor and trace element trends in the SMB. Additionally, the petrology of the samples collected is outlined.

Silica variation diagrams were plotted for all major elements of all sampled phases. The concentrations of Al_2O_3, Fe_2O_3, MnO, MgO, CaO and TiO_2 decrease with increasing SiO_2 content. In contrast, Na and K do not show any systematic variation with SiO_2. Silica variation diagrams were also plotted for trace elements to investigate their relationship to silica content. The concentrations of Ba, Hf, Th and Zr decrease with increasing SiO_2 content. The concentrations of U, Sn, and Ta increase with increasing SiO_2 content. These results are similar to those reported by MacDonald (2001) in a comprehensive study of the SMB geochemistry as a whole.

Table 2 Summary of whole-rock major element composition expressed in weight percentage **(wt. %)**

Sample	SiO2	Al2O3	Fe2O3(T)	MnO	MgO	CaO	Na2O	K2O	TiO2	P2O5	LOI	Total
18JC 0003	69.47	14.43	3.03	0.067	0.74	1.11	3.24	4.44	0.445	0.36	0.99	98.32
18JC 0004	72.13	13.78	2.04	0.05	0.42	0.81	3.39	4.59	0.266	0.25	0.83	98.56
18JC 0008	67.3	15.2	4.64	0.084	1.28	2.3	3.48	3.44	0.655	0.25	0.82	99.44
18JC 0010	69.28	14.39	3.64	0.072	0.88	1.38	3.07	4.48	0.465	0.21	0.95	98.82
18JC 0011	74.98	13.57	0.96	0.059	0.08	0.41	3.61	4.42	0.042	0.18	0.86	99.17
18JC 0016	74.41	13.51	1.24	0.051	0.06	0.37	3.68	4.07	0.038	0.3	0.83	98.57
18JC 0017	72.72	13.51	2.12	0.041	0.45	0.73	3.29	4.65	0.224	0.27	1.02	99.03
18JC 0019	74.5	13.5	2	0.046	0.11	0.43	2.26	3.99	0.071	0.36	1.54	98.8
18JC 0020	73.85	13.98	1.21	0.03	0.09	0.39	3.53	4.44	0.056	0.39	1.07	99.02
18JC 0021	68.38	14.01	4.46	0.072	1.14	1.58	2.97	4.07	0.613	0.22	1.03	98.56

Table 3 Summary of whole-rock REE concentration expressed in **ppm**

Sample	La	Ce	Pr	Nd	Sm	Eu	Gd	Tb	Dy	Ho	Er	Tm	Yb	Lu
18JC 0003	25	54.4	6.53	26.1	6	0.74	4.8	0.7	4	0.7	1.9	0.27	1.7	0.26
18JC 0004	18.8	41.5	5.03	19.3	4.5	0.52	3.6	0.5	2.7	0.4	1.2	0.17	1.1	0.18
18JC 0008	37.2	77.8	9.15	35.4	7.7	1.32	6.6	1	5.4	1.1	2.9	0.4	2.7	0.39
18JC 0010	28.4	60.8	7.23	27.7	6.5	0.91	5	0.9	5.2	1	2.8	0.44	2.8	0.41
18JC 0011	2.5	6.5	0.83	3.3	1.3	< 0.05	1.2	0.3	1.8	0.4	1.1	0.19	1.4	0.2
18JC 0016	2.2	6.4	0.86	3.3	1.3	< 0.05	1.2	0.3	1.6	0.3	0.9	0.17	1.2	0.17
18JC 0017	16.1	37.1	4.39	17.2	4.4	0.42	3.4	0.6	2.8	0.4	1.2	0.16	1	0.14
18JC 0019	4.4	8.5	0.99	3.7	1	< 0.05	0.9	0.2	1.2	0.2	0.5	0.08	0.5	0.07
18JC 0020	2.3	5.5	0.67	2.8	0.9	0.05	0.8	0.2	0.9	0.1	0.4	0.05	0.4	0.01
18JC 0021	34.3	73	8.88	34.8	8.4	1.11	7.2	1.1	6.6	1.2	3.1	0.43	2.6	0.42
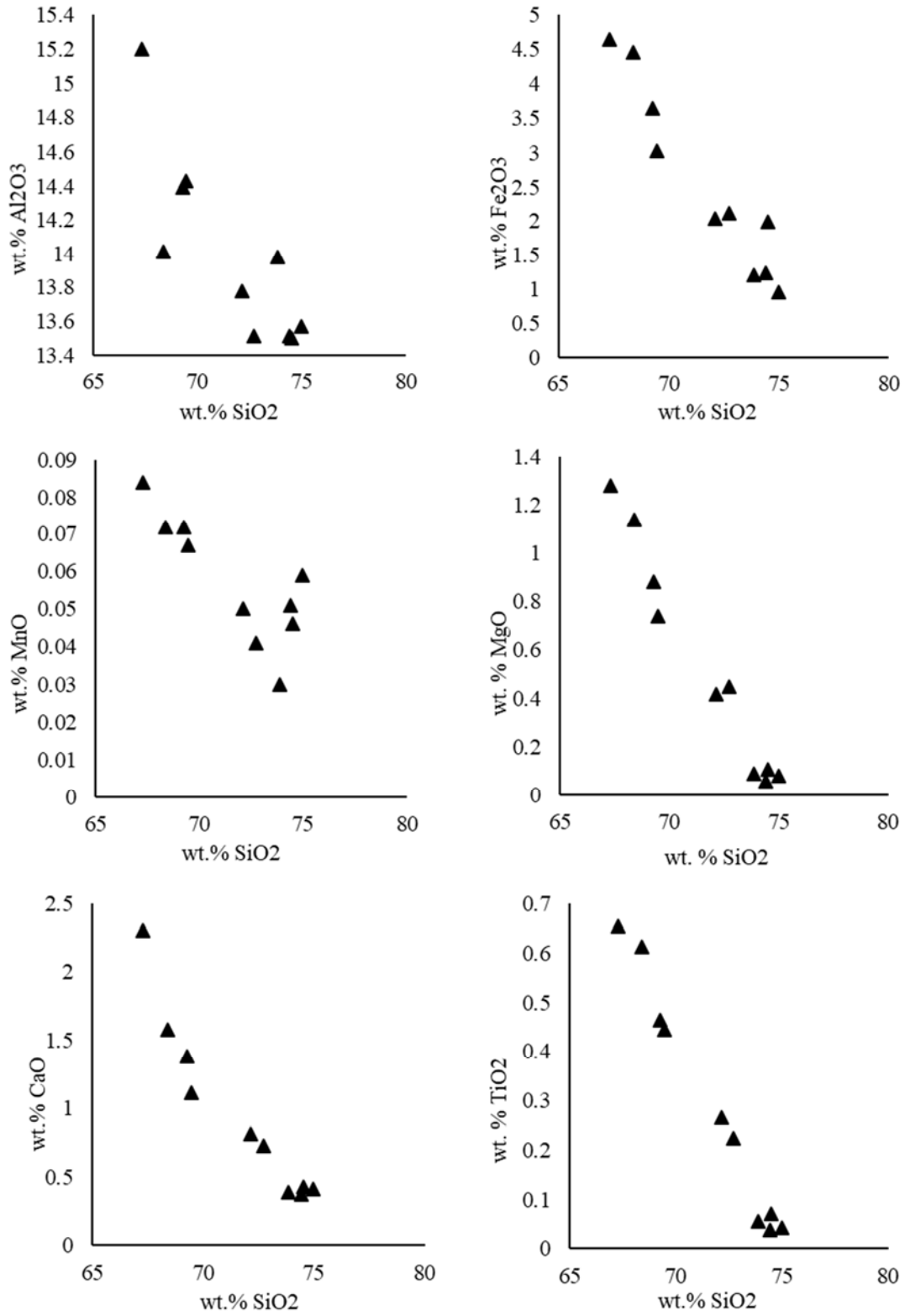
Figure 9. Harker diagrams plotting SiO_2 wt % vs other oxide concentrations expressed in wt %.
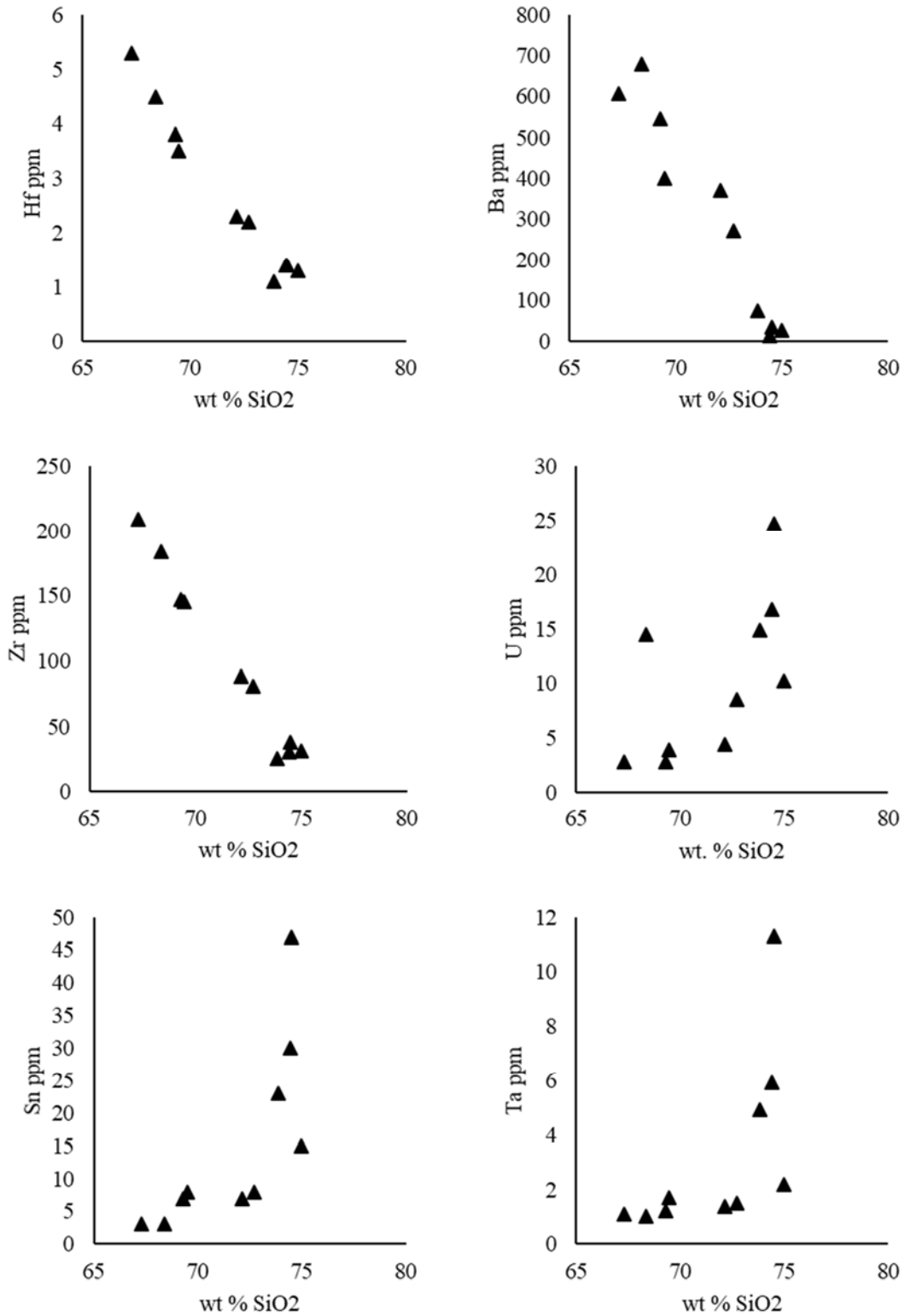
Figure 10. Harker diagrams plotting SiO_2 wt % vs trace element concentrations expressed in ppm

Whole rock chondrite-normalized REE diagrams were plotted for all sampled phases. All samples show a LREE/HREE >> 1 and significant negative europium anomalies. The geometry of the trends and the presence of the Eu anomaly are consistent with the results summarized in MacDonald (2001).
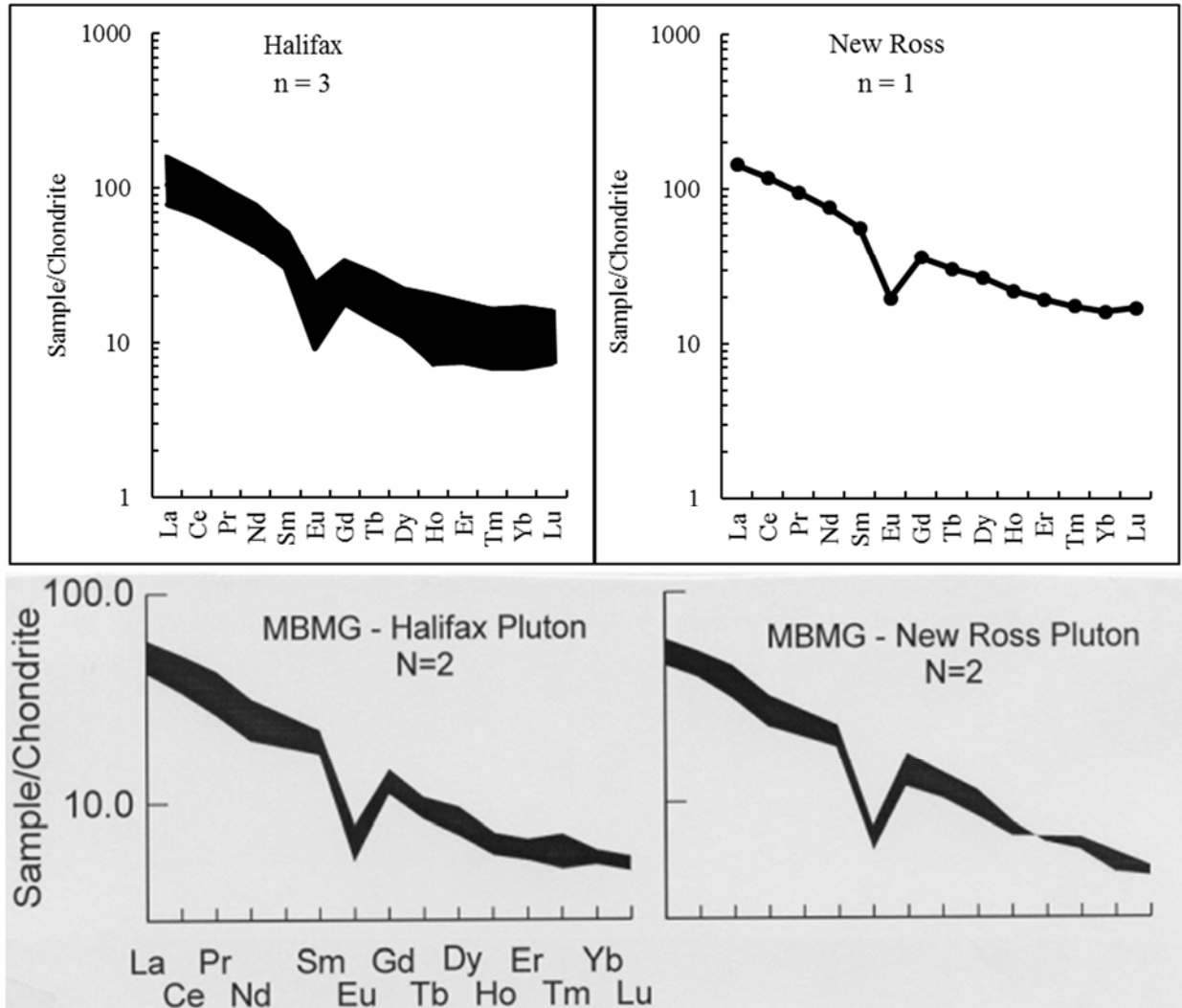
Figure 11 Chondrite normalized REE profiles for this study (top) and MacDonald, 2001 (bottom)

Variation diagrams for trace elements were also plotted in order to compare this study's results to those of Muecke and Clarke (1981). These diagrams plot a variety of trace element against the sum of 7 selected REE. The aim of these plots is to depict the systematic variation of compatible (Ba and Zr) and incompatible (Rb and Ta) trace elements with respect to REE. The concentration of compatible trace elements seems to increase with increase in $\sum 7REE$. Incompatible trace elements appear to have the opposite trend.
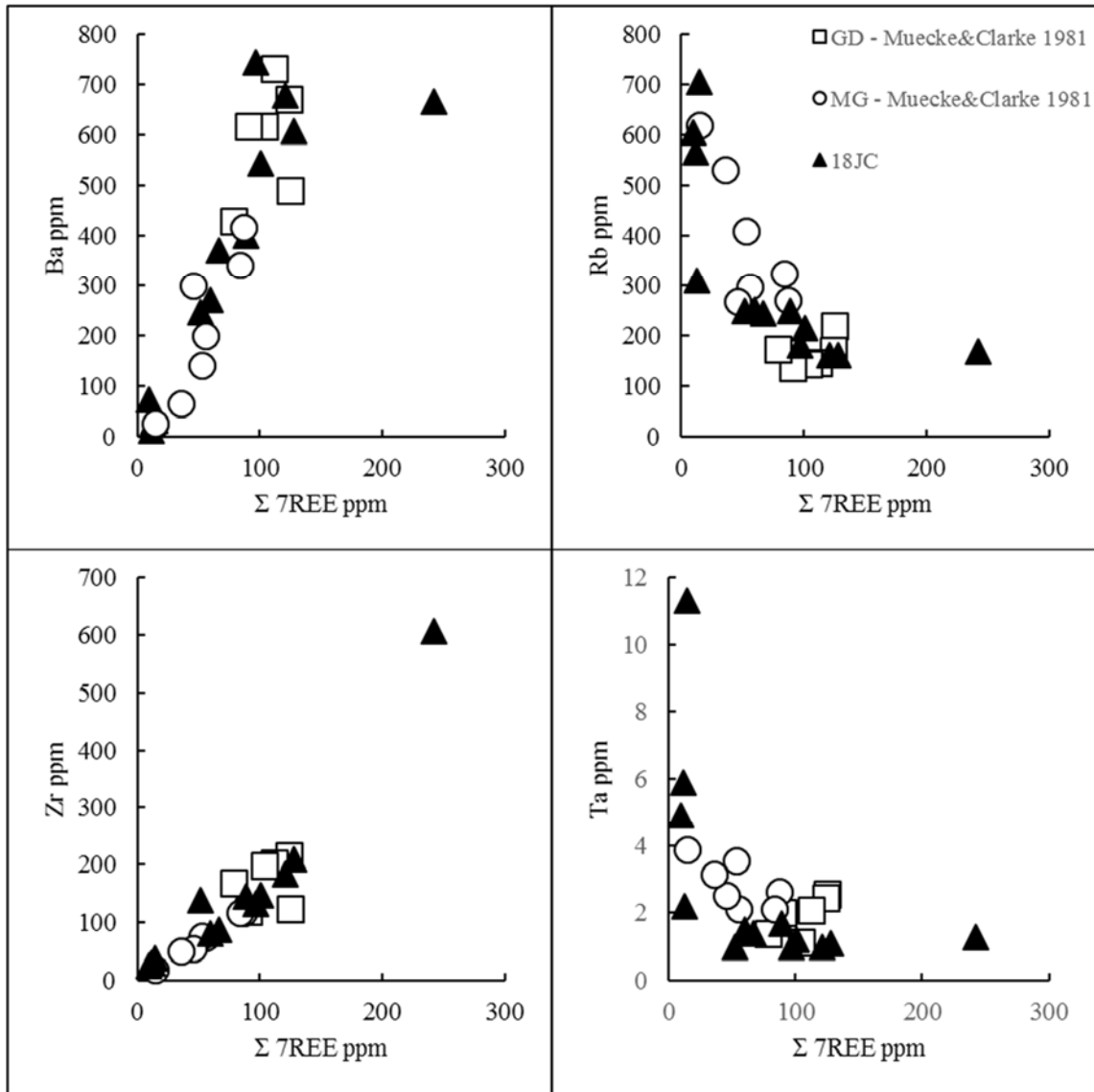
Figure 12 . 7REE vs. HSFE and LILE variation diagrams, modified from Muecke & Clarke, (1981). Open squares labelled 'GD' correspond to individual granodiorite samples from Muecke & Clarke, (1981). Open circles labelled 'MG' correspond to individual monzogranite samples from Muecke & Clarke, (1981). Closed triangles correspond to all phases of this study.

4.2 Petrography

Petrographic observations were made to determine the identity, modes and textural relations amongst the minerals present. The dominant minerals in all phases are quartz, alkali feldspar, plagioclase and biotite. All but one sample fall within the monzogranite field of the QAPF based on modal mineralogy. The outlier falls within the syenogranite field. The samples show moderate textural variation but are primarily inequigranular and contain both euhedral and anhedral phenocrysts. Most samples show some degree of chloritization of biotite and

sericitization of feldspars, particularly plagioclase. Perthitic texture in alkali feldspars and graphic textures associated with quartz and feldspars are also common. More detailed petrography of individual samples can be found in the Appendix.
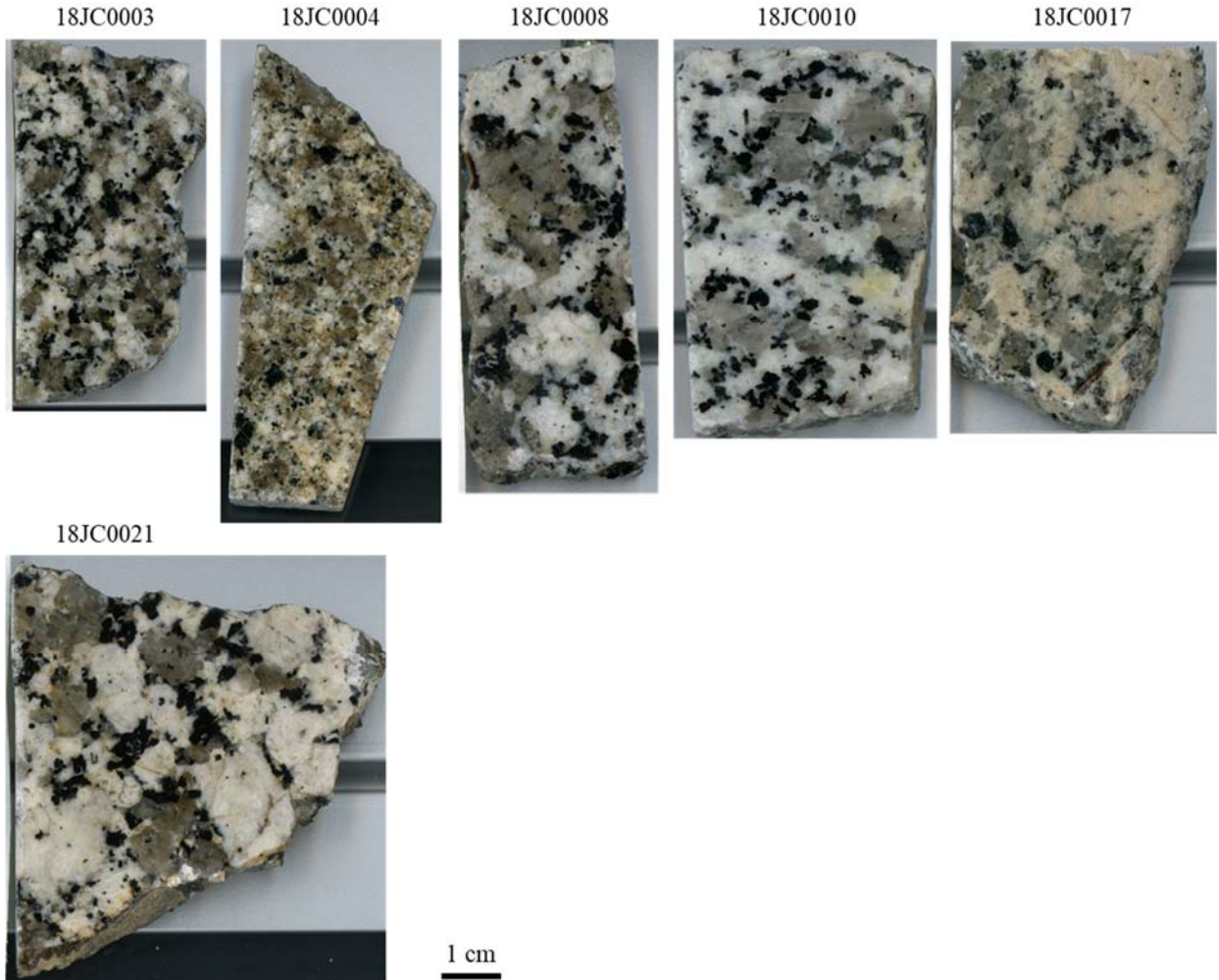
Figure 13 Hand sample specimens from each analysed phase of the SMB. 18JC0003, 18JC0004 and 18JC0008 correspond to the unmineralised Halifax pluton. 18JC0010 and 18JC0017 correspond to the Sandy Lake pluton. 18JC0021 corresponds to the mineralised New Ross pluton.

All zircon observed in these samples exists as inclusions within rock-forming minerals, as opposed to along grain boundaries or interstitial spaces between other grains. The most common host for zircon is biotite (altered and unaltered), closely followed by quartz. Zircon inclusions in plagioclase are rare and no inclusions were observed in alkali feldspar. Zircon crystals observed in thin section range from >0.1-0.4 mm and are both euhedral and anhedral. The main optical characteristics used to distinguish zircon are its very high positive optical relief and 2nd to 3rd order

interference colours. A more detailed morphological description of zircon crystals is presented in the following section.
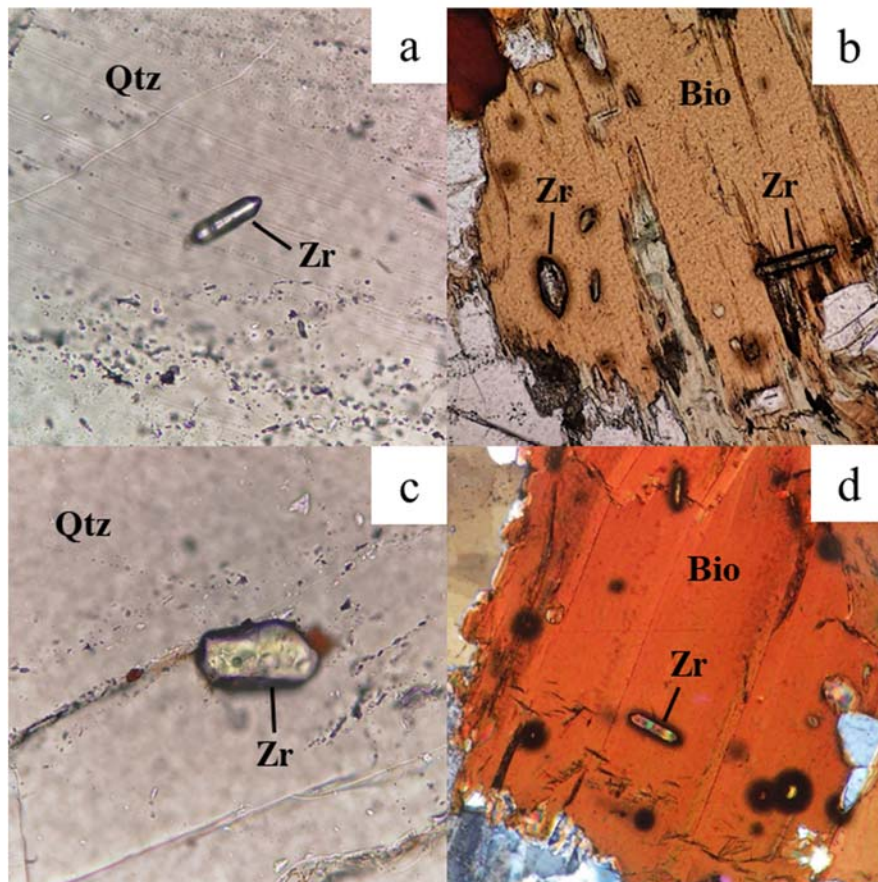
Figure 14 Examples of zircon crystals in the SMB. (a) Euhedral zircon inclusion in quartz from unmineralised granite (sample 18JC003). (b) Euhedral and anhedral zircon inclusions in chloritized biotite from unmineralised granite (sample 18JC0004). (c) Anhedral zircon inclusion in quartz from mineralised granite (sample 18JC0021). (d) Euhedral zircon inclusion in unaltered biotite from mineralised granite (sample 18JC0021). Zircon grains are ~100 microns in long dimension.

4.2 Zircon Morphology and Geochemistry

Upon examination of CL-images, petrography, and geochemical data, it became apparent that zircon in the SMB shows distinct groupings in terms of morphology and trace element composition, similar to that documented in Yang et al, (2014). Zircons were classified as either "magmatic" or "non-magmatic", with the latter subdivided into metamict or hydrothermal. The defining characteristics are outlined in Table 4. These differences are thought to be a product of different crystallisation media and temperature, as well as interaction with fluids (Yang et al, 2014). These differences are manifested in a variety of features, such as morphology, rock-type

association and, most importantly, their REE distribution. The following section will aim to highlight these features and compare magmatic and non-magmatic zircon of the SMB.

Table 4 . Summary of distinctive features in magmatic, metamict and hydrothermal zircon from Yang et al, 2014.

Zircon	Magmatic zircon	Metamict zircon	Hydrothermal zircon
T (-P) conditions	High temperature (>650 °C)	High to low temperature	Low temperature (<500 °C)
Crystallization medium	Magmatic melt	Crystallized in magmatic melt and altered by deuteric hydrothermal fluid	Magmatic–hydrothermal transition
Crystallinity	Well crystallized	Amorphous	Well crystallized
Host rock	Fine-grained barren granite	Coarse-grained mineralized granite	Coarse-grained mineralized granite
Textural features	Small sized (<0.03 × 0.1 mm)	Small sized (<0.03 × 0.1 mm)	Large sized (>0.1 × 0.1 mm)
	Oscillatory zoned	Mostly murky	Murky and featureless
	Inclusion-rich	Inclusion-rich	Inclusion-poor
Geochemical features	Depleted in LREE	Relatively enriched in P and REE, especially U, Th, and HREE	Enriched in LREE, Nb, Ta, Ti, Hf, Th, and U
	Low LREE/HREE ratios (<0.07) and high Th/U ratios (mostly >0.4)	Low LREE/HREE ratios (<0.02) and high Th/U ratios (mostly >0.3)	High LREE/HREE ratios (>0.1) and low Th/U ratios (mostly <0.3)
	Significant positive Ce-anomaly and negative Eu-anomaly	Weak positive Ce-anomaly, strong negative Eu-anomaly and notable M-type REE tetrad effect	Weak positive Ce-anomaly, strong negative Eu-anomaly and notable M-type REE tetrad effect
	Geothermometer available	Maybe suitable for Ti-in zircon geothermometer	Not suitable for Ti-in zircon geothermometer

4.2.1 Zircon Morphology

      Zircon from samples collected for this project generally range in size from > 10 μm to 350 μm. CL-imaging was performed to place the chemical analyses into textural context and characterize individual zircon morphologies. The following figures provide examples of textures associated with magmatic and non-magmatic zircon according to the classification scheme of Yang et al (2014).
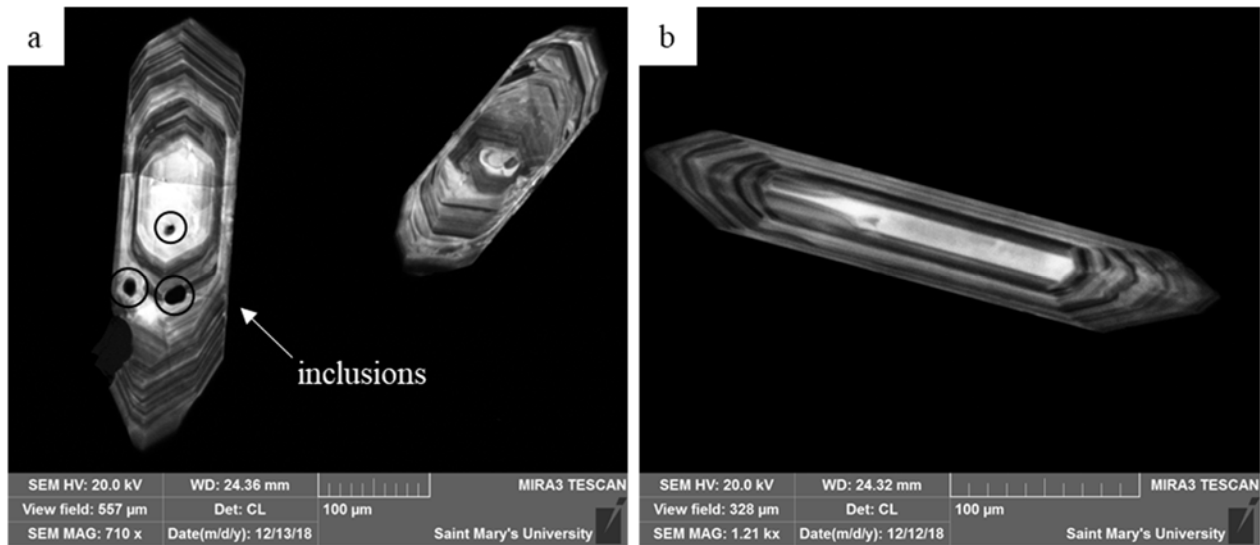
Figure 15 Cl-images of zircon showing "magmatic" characteristics, as defined by Yang et al, (2014). (a) Sample 18JC0008, monzogranite from the Halifax Pluton. (b) Sample 18JC0021, monzogranite from the New Ross Pluton.

      The crystals in Figure 15 are euhedral and small, 100 – 300 μm on longest axis. The crystal Cl response shows concentric oscillatory zoning that is largely uninterrupted or truncated. Finally, zircon that have been interpreted to be magmatic typically contain inclusions, likely of apatite and quartz. The crystals shown in Figure 15 are interpreted to be magmatic based on their morphology and REE profile.
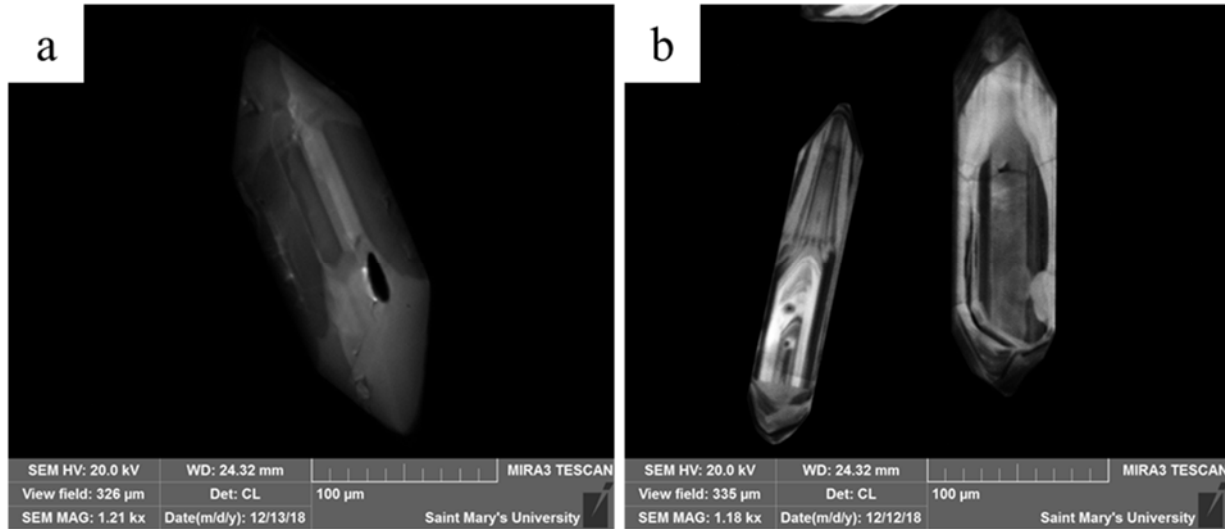
Figure 16 Cl-images of zircon showing "non-magmatic" characteristics, as defined by Yang et al, (2014). (a) Sample 18JC0004, monzogranite from the Halifax Pluton. (b) Sample 18JC0021, monzogranite from the New Ross Pluton.

Zircons shown in figure 16 are relatively large, from 100-500 μm on longest axis, and lack well developed oscillatory zoning. They also have distinct REE profiles (see below, Figure 17). The characteristics of these zircons are consistent with those of the non-magmatic variety of Yang et al, (2014).

4.2.2 REE Distribution

Figure 17 shows chondrite-normalized REE plots for unmineralised (Halifax and Sandy Lake) and mineralised (New Ross) samples. Magmatic and non-magmatic zircon types from the SMB have significantly different absolute and relative REE concentrations (Figure 17). The cerium anomaly (Ce/Ce*), which is the total concentration of cerium over Sm/La, is one of the important differences between magmatic and non-magmatic zircon. Magmatic zircon exhibit strong positive cerium anomalies, with an average Ce/Ce* value of 14.8. The average Ce/Ce* value for non-magmatic zircon is an order of magnitude lower, at 1.7. This difference is clearly seen in Figure 17, which do not show significant cerium anomalies in non-magmatic samples.

HREE concentrations are similar for all zircon (Figure 17), but magmatic zircon is significantly depleted in LREE with respect to non-magmatic zircon. This relationship can be described by the Sm/La ratio, which is the slope of the LREE portion of the profile. The magnitude of the ratio is inversely proportional to the concentration of La, and therefore, samples that are depleted in La will exhibit the largest ratios. The average Sm/La value for non-magmatic zircon is 14.5, while the value for magmatic zircon is 518.3.

29

Figure 18 portrays the variation of Ce/Ce* with Sm/La, similar to that of Yang et al, (2014). This graph illustrate the differences between magmatic and non-magmatic zircon with respect to these ratios. The Ce/Ce* value for magmatic and non-magmatic zircon ranges from 2 to 1000 and from 0.1 to 100, respectively. The Sm/La value for magmatic and non-magmatic zircon ranges from 5 to 10000 and 1 to 1000, respectively. Variation in both types of zircon is similar for both parameters, but magmatic zircon is shifted to higher Sm/La and generally higher Ce/Ce*.
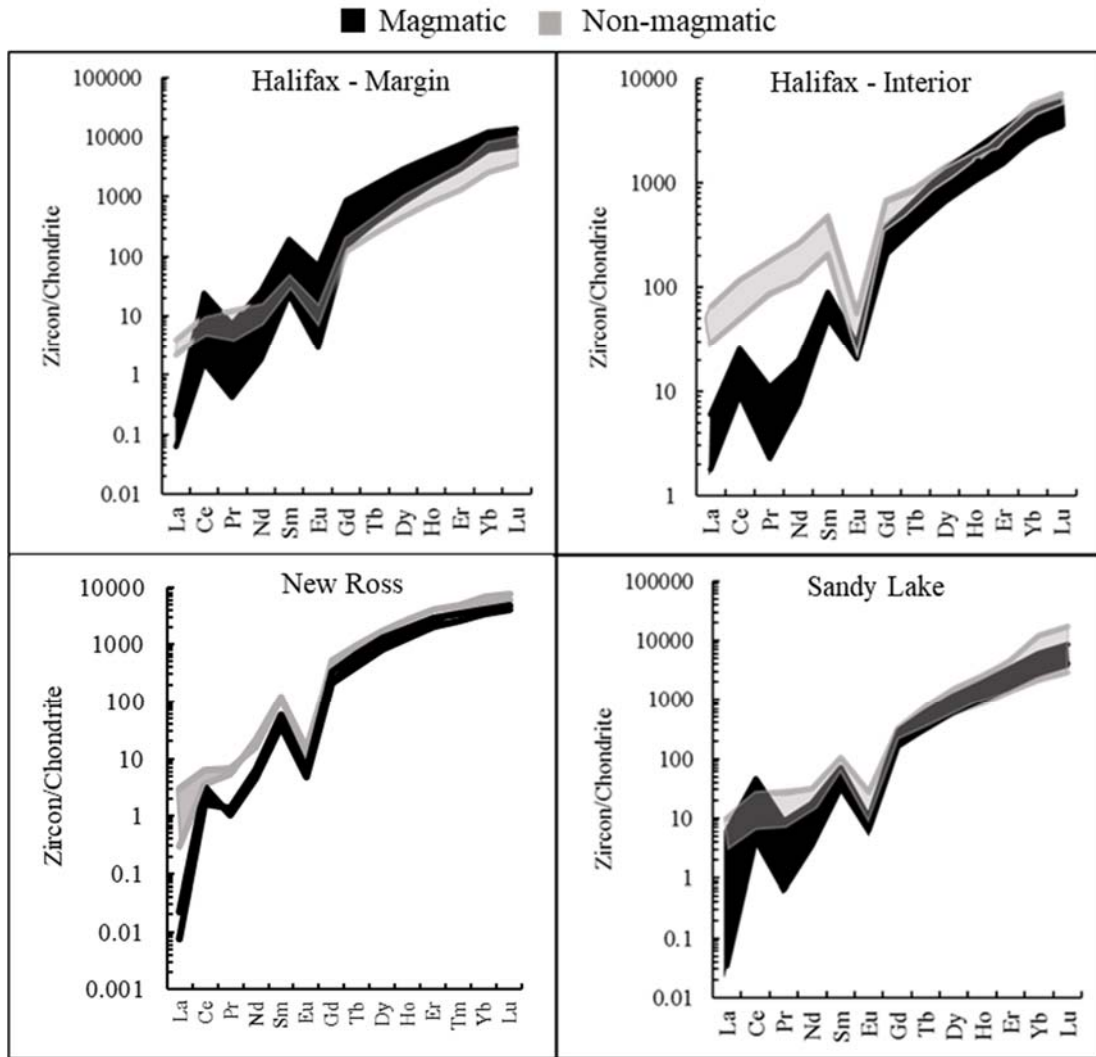
Figure 17 Chondrite-normalized REE diagrams for zircons analysed in this study from three different plutonic phases of the SMB. The data are subdivided into magmatic and non-magmatic textural types.
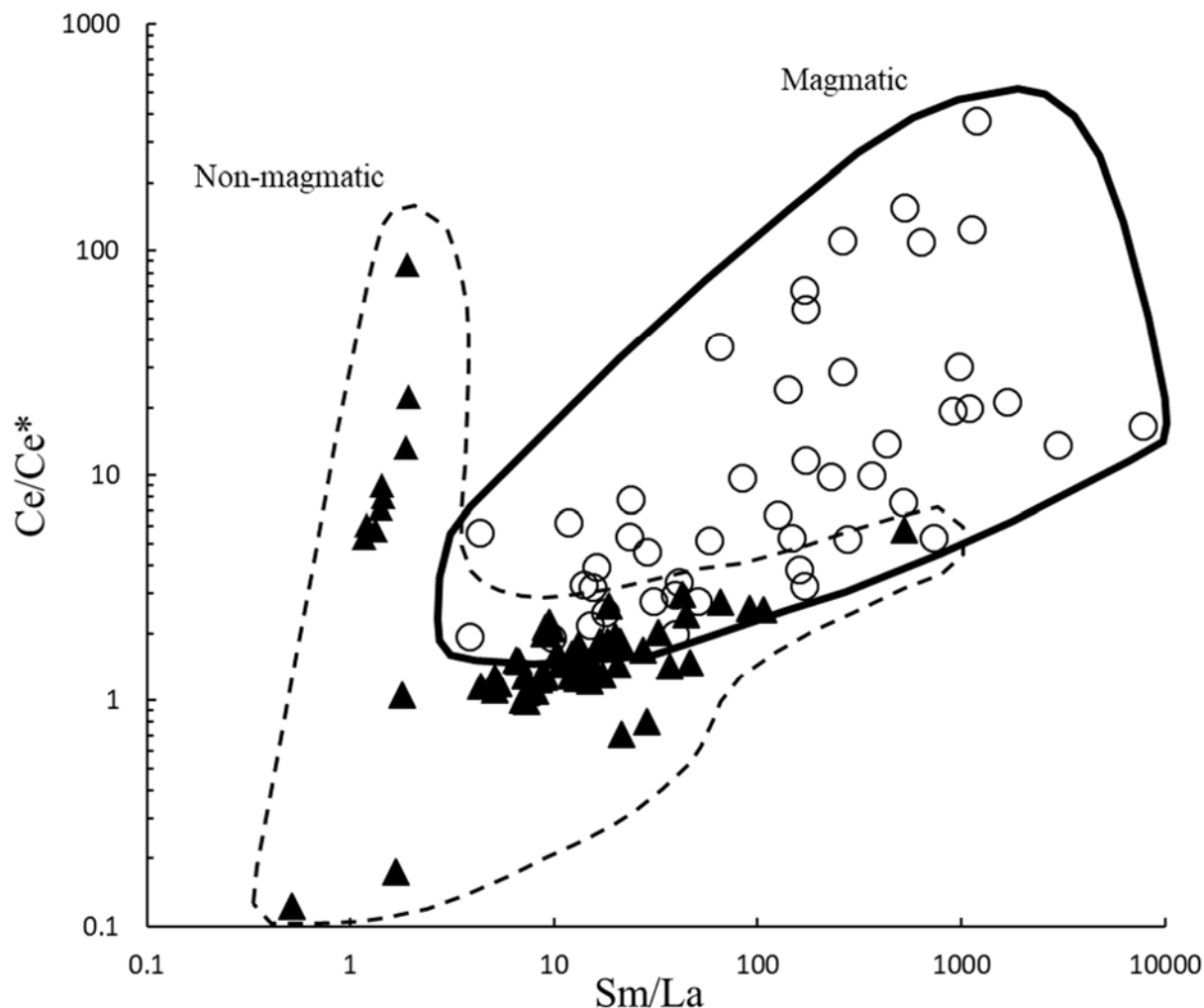
Figure 18 Ce/Ce* vs. Sm/La plot after that of Yang et al, (2014). Open circles represent zircon analyses that exhibit magmatic REE profiles. Closed triangles represent zircon analyses that exhibit non-magmatic REE profiles. Region enclosed by solid line corresponds to magmatic zircon. Region enclosed by dashed line corresponds to non-magmatic zircon

As further evidence in support of the magmatic zircon interpretation, the distribution of REE for individual analyses was also examined by comparison to data from Sano et al, (2002). Sano et al, (2002) provide well-constrained $D_i^{zircon/melt}$ for REEs of zircon in equilibrium in a natural system. In theory, $D_i^{zircon/SMB}/D_i^{zircon/Sano}$ should yield ratios of 1:1 or x:1 if the analyses are in equilibrium with the whole rock. The resulting ratios were plotted, and ratios that seem to show a 1:1 or x:1 relationship were selected. This list of analyses was then cross-referenced with zircons that were considered to be magmatic based on the characteristics discussed previously in this section. The resulting reduced list was utilized on section 4.3.

4.2.3 Zircon Trace Element Geochemistry

Uranium and Hf were examined to compare their concentrations in zircon and whole rock. The average concentration of these elements in zircon from all phases was calculated and plotted as a function of SiO_2. The concentration of uranium in zircon, like in whole rock, increases with silica content. Hafnium, however, exhibits the opposite trends when comparing whole rock and zircon distributions. Other elements such as Th, Ta and Ba were examined, but did not exhibit perceivable trends in zircon.
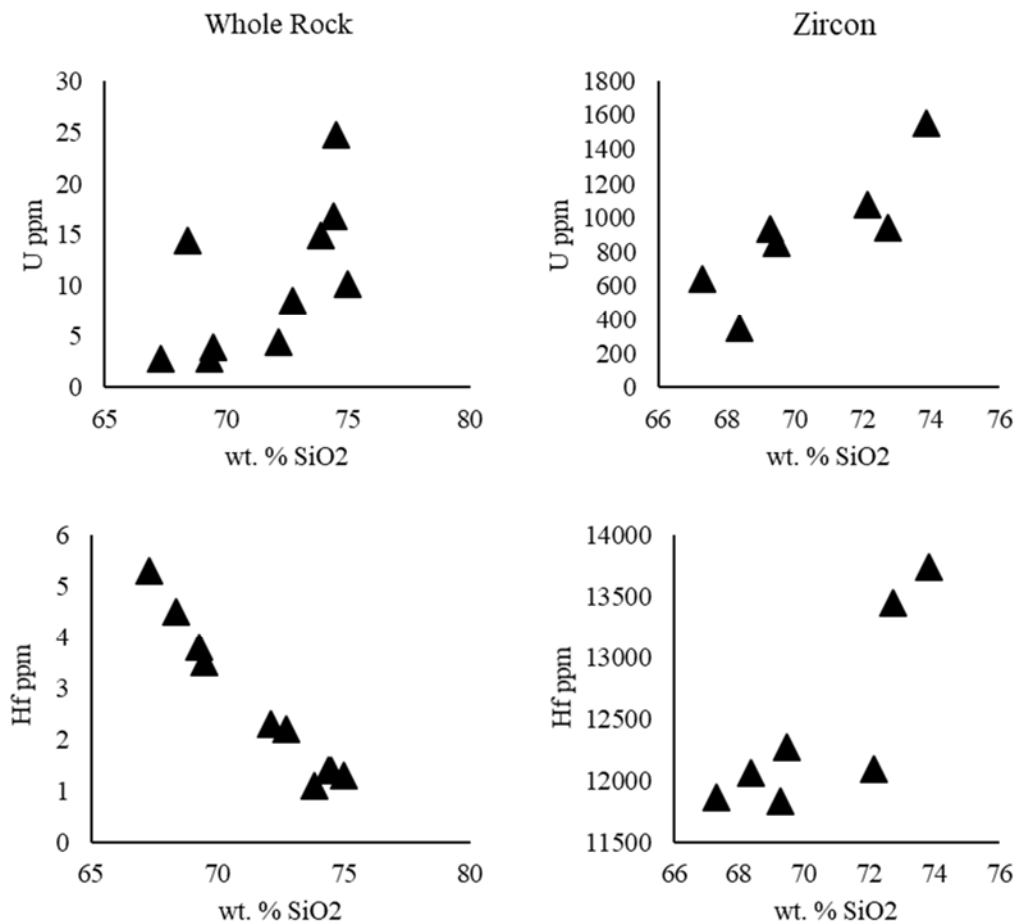
Figure 19 Silica variation diagrams for U and Hf for whole rock and zircon

4.3 Oxygen Fugacity

Oxygen fugacity was determined from the composition of magmatic zircon following the method of Smythe and Brenan (2016). This method requires accurate estimations of: activity of SiO_2, activity of TiO_2, and wt% of water dissolved in the melt. Furthermore, filters used to discriminate between magmatic and non-magmatic, and zircon in equilibrium with whole rock

were applied to address inconsistencies in the data. The following section aims to provide justification for these estimations and filters, and provide fO₂ values that appear to be reliable.

4.3.1 Activity of SiO₂, TiO₂, and Dissolved H₂O

The Ferry & Watson, (2007) Ti-in-Zircon geothermometer is used to determine zircon crystallization temperature. This method makes use of the strong temperature dependence of the Ti content of zircon when the external activities of SiO₂ and TiO₂ are fixed. The temperature can be determined from the following equation (Ferry & Watson, 2007):

$$\log(\text{ppm Ti} - \text{in} - \text{zircon}) = (5.711 \pm 0.072) - \frac{(4800 \pm 86)}{T(K)} - \log a_{SiO_2} + \log a_{TiO_2}$$

Equation 3

For the purpose of this calculation, it was assumed that [SiO₂] and [TiO₂] are unity. Although the assumption of [SiO₂] = 1 is validated by the presence of modal quartz, rutile was not observed in these samples. However, Clarke & Carruzzo, (2007) and MacDonald, (2001) state that rutile is a ubiquitous magmatic phase in the SMB, and therefore an assumption of [TiO₂] = 1 is reasonable.

A more difficult quantity to estimate in plutonic rocks is their water content. In this case, it is assumed that samples crystallized zircon under water-sasturated conditions at the estimated pressure of emplacement of 400 MPa (Mackenzie & Clarke, 1974). Graphic quartz and alkali feldspar intergrowth, miarolitic cavities, abundant pegmatites, and ring schlieren (Clarke et al, 2013) are all associated with water saturation (Clarke et al, 2013; see also the discussion in Kontak, 1990).

The water content at saturation was determined from the experimental data summarized by Holtz et al, (1995) for 'haplogranitic' compositions, which is similar to the natural samples collected for this study. As shown in Figure 20, the effect of temperature on water solubility is minor, and a value of 9 wt% is used based on the estimated emplacement depth. The oxygen fugacity of analysed zircons was also calculated for water contents of 5%, as well as, for [TiO₂] = 0.5 to test the sensitivity of the calculated *f*O₂ on these parameters.
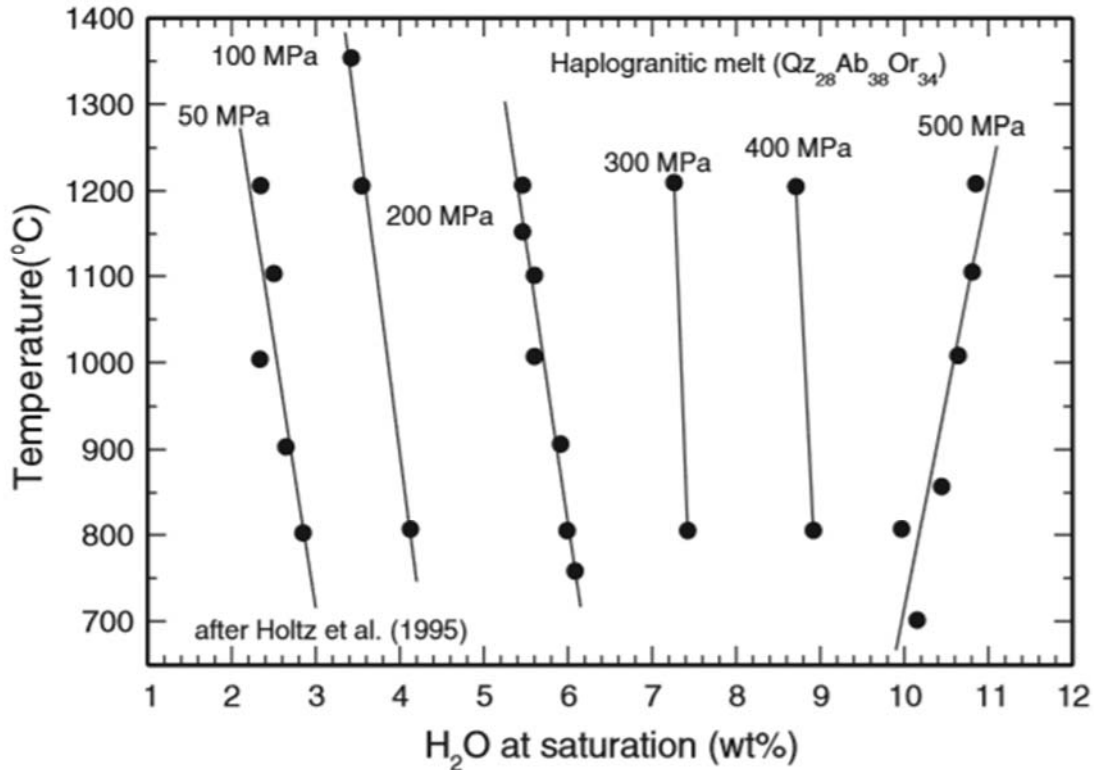
Figure 20 Experimental data from Holtz et al (1995) showing the variation in dissolved H_2O at saturation as a function of temperature and pressure.

4.3.2 Calculated Oxygen Fugacities and Temperatures

Calculated oxygen fugacities of magmatic zircons are presented in Table 5, along with temperatures, using the assumed values for $[SiO_2]$, $[TiO_2]$ and water content. These oxygen fugacities correspond to zircons that are considered to be magmatic and in equilibrium with the whole rock as defined in section 4.2.

In terms of the sensitivity of these parameters, decreased H_2O content shifts the calculated fO_2 to lower values. This is illustrated in Figure 22, which is a series of histograms for calculated ΔFMQ at different conditions. Notably, the peak frequency for calculations at 5% H_2O is 1.5 log units more reducing than the peak frequency for calculations at 9% H_2O. A decrease in the $[TiO_2]$ from 1 to 0.5 has a relatively minor effect on calculated fO_2, shifting values by approximately 0.25 log units.

Temperature calculations are independent of water content, but do vary with $[TiO_2]$; a decrease in the activity of TiO_2 from 1 to 0.5 shifts the calculated equilibration temperature to higher values (+60ºC or so) and results in a small shift (~0.2 log units) in ΔFMQ to more reduced

34

values. Therefore, the concentration of dissolved water has a stronger influence on the calculated fO_2 than temperature for the analysed zircons of the SMB.

The oxygen fugacity recorded by zircons assuming 9 wt% H_2O in the melt varies both among different plutons and within single plutons (Table 5; Figure 21). For samples from the interior of the Halifax pluton, ΔFMQ varies from -3.2 to 2.5, with an average of -0.2. Samples from the margin of the Halifax pluton, yielded ΔFMQ values from -3.3 to 0.2, with an average of -1.2. ΔFMQ of the Sandy Lake pluton varies from 0.2 to 0.6 and has an average 0.4. Finally, the ΔFMQ recorded by the mineralised New Ross pluton varies from -3.8 to -0.5 and has an average of -2.1.

Table 5 Summary of fO$_2$ calculations under different conditions. Conditions for H$_2$O 5% are H$_2$O wt% = 5 and [TiO$_2$] = 1.0. Conditions for H$_2$O 9% are H$_2$O wt% = 9 and [TiO$_2$] = 1.0. Conditions for TiO$_2$ 0.5 are H$_2$O wt% = 9 and [TiO$_2$] = 0.5.

		H$_2$O 5%		H$_2$O 9%		TiO$_2$	
Pluton	Sample	T ( )	ΔFMQ	T ( )	ΔFMQ	T ( )	ΔFMQ
Halifax	18JC0003_7a	728.686	-0.703	728.686	0.764	795.83	0.634
	18JC0003_10a	660.981	1.047	660.981	2.513	719.092	2.379
	18JC0003_10b	652.345	-4.649	652.345	-3.182	709.354	-3.317
	18JC0003_27a	702.468	-3.302	702.468	-1.836	766.032	-1.966
	18JC0003_27b	661.824	-0.339	661.824	1.128	720.043	0.994
	18JC0004_1a	751.395	-0.808	751.395	0.648	821.725	0.519
	18JC0004_2b	739.121	-1.828	739.121	-0.373	807.719	-0.502
	18JC0004_7a	800.717	-3.505	800.717	-2.05	878.239	-2.179
	18JC0004_13a	748.676	-1.229	748.676	0.227	818.62	0.098
	18JC0008_8a	815.978	-1.337	815.978	0.123	895.801	-0.006
	18JC0008_9a	760.109	-2.092	760.109	-0.633	831.683	-0.761
	18JC0008_18a	690.657	-2.07	690.657	-0.61	752.642	-0.742
	18JC0008_18b	657.753	-4.562	657.753	-3.102	715.45	-3.236
	18JC0008_20a	726.811	-1.635	726.811	-0.175	793.695	-0.305
	18JC0008_24a	714.707	-3.372	714.707	-1.913	779.929	-2.043
	18JC0008_27a	724.676	-1.225	724.676	0.235	791.266	0.105
	18JC0008_27b	608.351	-4.787	608.351	-3.327	659.917	-3.466
Sandy Lake	18JC0010_1a	873.336	-1.247	873.336	0.217	962.132	0.086
	18JC0010_10a	728.357	-0.87	728.357	0.593	795.456	0.464
	18JC0010_11a	949.721	-0.985	949.721	0.478	1051.269	0.34
Ne Ross	18JC0021_1b	771.752	-3.996	771.752	-2.528	845.005	-2.657
	18JC0021_4b	762.497	-1.924	762.497	-0.456	834.414	-0.585
	18JC0021_9a	664.919	-5.227	664.919	-3.759	723.536	-3.892
	18JC0021_25b	701.205	-3.037	701.205	-1.57	764.599	-1.7
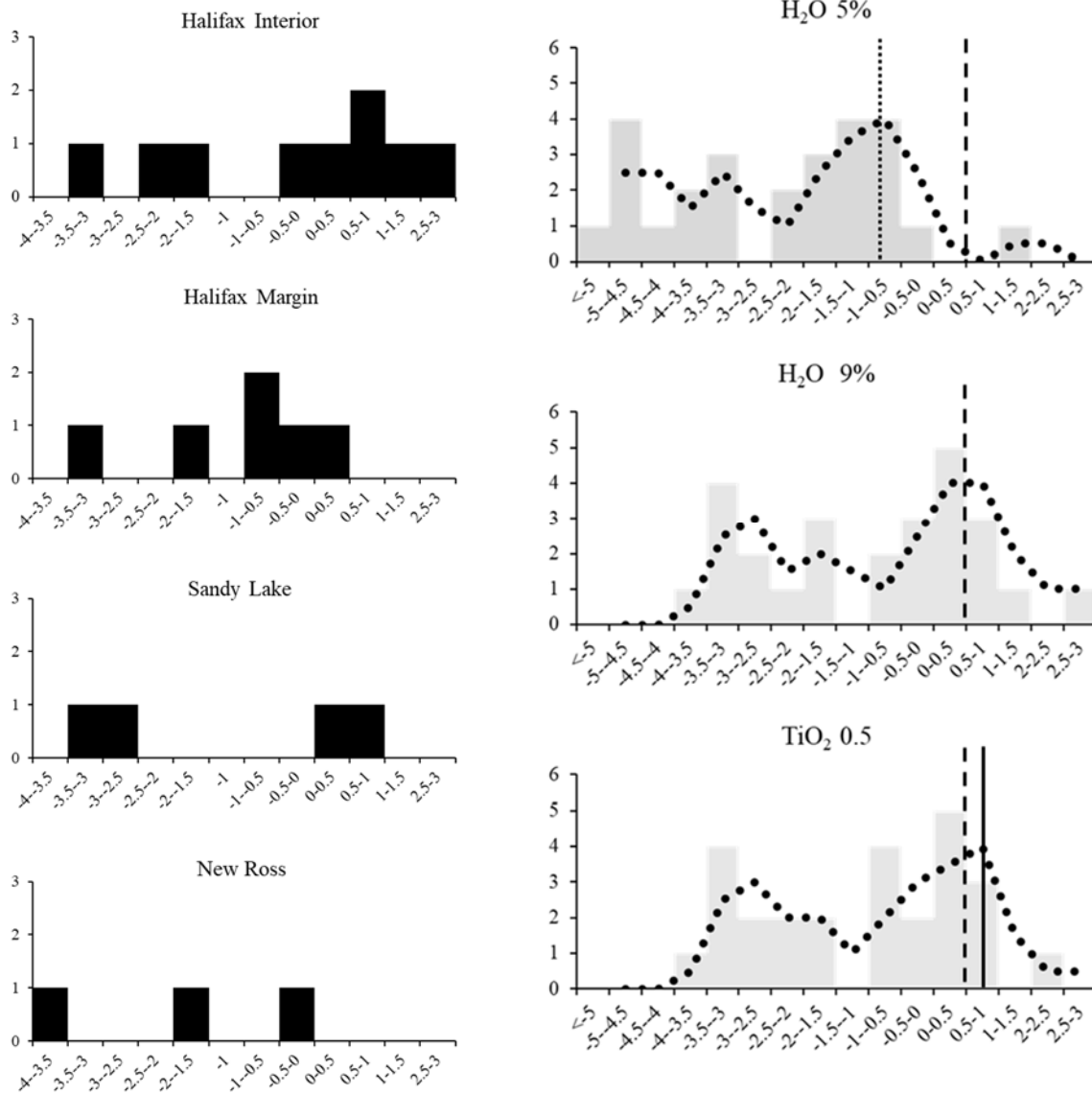
Figure 21. (left) ΔFMQ histogram for individual plutons of all analysed samples in Table 5. Frequency range for all plots is 0 to 3 and ΔFMQ range for all plots is -4 to 3. (right) ΔFMQ histogram for all analysed samples at different melt conditions. Conditions for 'H$_2$O 5%' are H$_2$O wt% = 5 and [TiO$_2$] = 1.0. Conditions for 'H$_2$O 9%' are H$_2$O wt% = 9 and [TiO$_2$] = 1.0. Conditions for 'TiO$_2$ 0.5' are H$_2$O wt% = 9 and [TiO$_2$] = 0.5. Dotted line represents peak frequency of ΔFMQ for 'H$_2$O 5%'. Dashed line represents peak frequency of ΔFMQ for 'H$_2$O 9%'. Solid line represents peak frequency of ΔFMQ for 'TiO$_2$'.

Chapter 5. Discussion

5.1 Comparison between fO₂ for the SMB and other Igneous Rocks

Although there is considerable variation, the average ΔFMQ value for the SMB is -0.95, which serves for the purpose of comparison with other igneous rock suites. The range of oxygen fugacity values observed in mafic igneous rocks, from Mid-Ocean Ridge Basalts (MORBs) to lamprophyres, extends over 7 orders of magnitude, which is the largest variation of any intensive parameter in petrology (Carmichael & Ghiorso, 1990). Mallman & O'Neill, (2009) report a ΔFMQ range of 0.5 to -1.5 for oceanic basalts, including MORBs, oceanic island basalts and island arc basalts. Carmichael (1991) presents data for lamprophyric lavas of western Mexico that plot in the opposite end of the spectrum at ΔFMQ values near +5. The range of ΔFMQ values observed in silicic magmas is smaller (Carmichael & Ghiorso, 1990). The most reduced silicic suites are as reduced as MORBs, but the most oxidized suites reach ΔFMQ values of +2 (Carmichael, 1991). This implies the expected range of fO_2 values in silicic rocks is ΔFMQ ±2. Therefore, ΔFMQ values obtained in this study place the SMB within the expected range of all igneous rocks, and towards the reduced end of silicic magmas.

Relevant literature often describes the redox state of granitic bodies in terms of magnetite- and ilmenite-series, as these minerals mark the distinction between oxidized and reduced conditions, respectively (Sasaki & Ishihara, 1979). Magnetite-series granitoids, such as the Cadia Igneous Complex and the Glenbog Supersuite of the Lachlan Fold Belt (LFB) in Australia, are moderately to strongly oxidized (Belvin, 2004). Ilmenite-series anorogenic granitoids, such as the Pikes Peak and Wolf River batholiths, straddle the FMQ buffer and have ΔFMQ values of 0 to -1 (Anderson, 1983). Ilmenite-series orogenic granitoids, such as the Strathbogie Batholith of the LFB, are also reduced (Phillips et al, 1981). The Strathbogie batholith, like the SMB, has been interpreted to be dominantly post-collisional, contains magmatic cordierite and is classified as peraluminous (Phillips et al, 1981). Additionally, it has an approximate ΔFMQ of -1 (Phillips et al, 1981), which is remarkably similar to the SMB. It appears that zircon from the SMB records a similar redox state to other ilmenite-series granites.
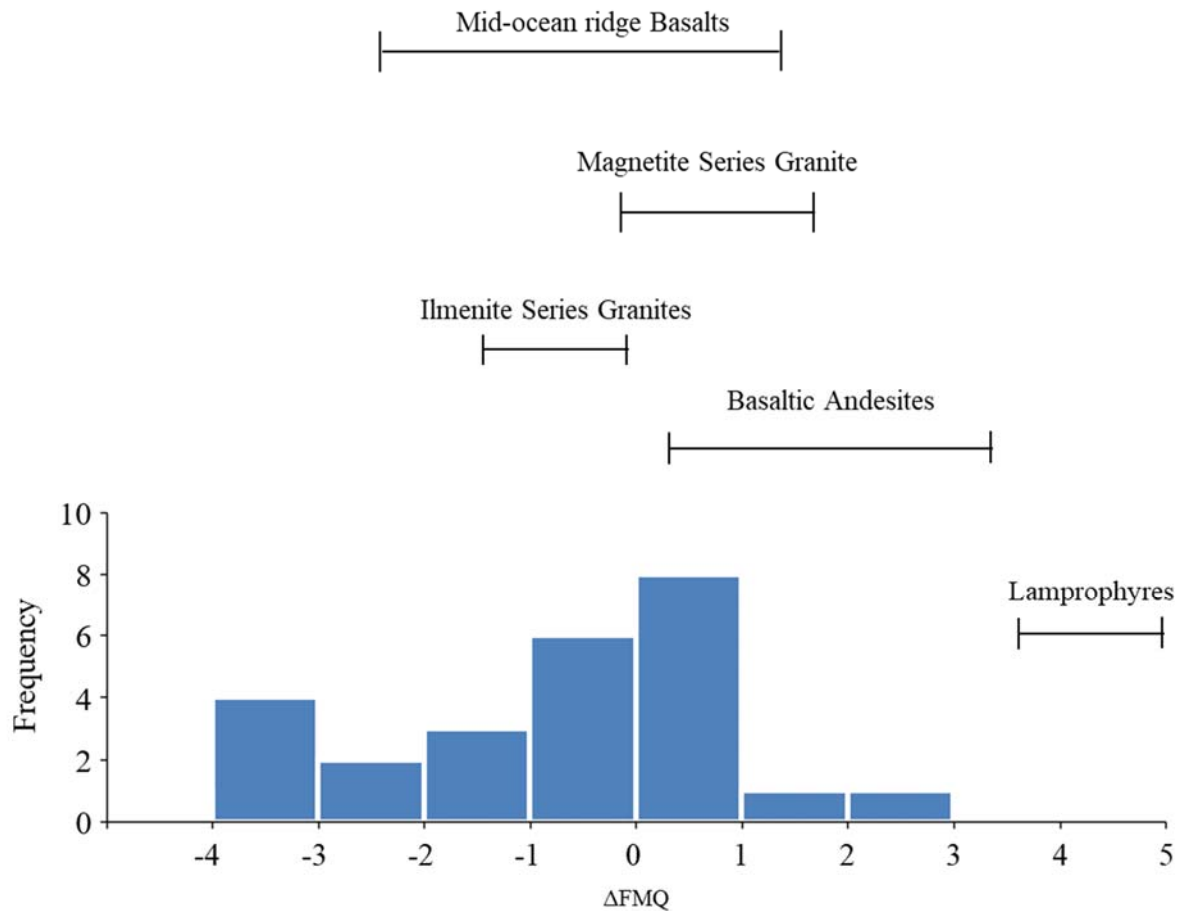
Figure 22. Histogram of ΔFMQ values obtained from the SMB samples of this study compared to ranges recorded by oceanic basalts (Mallman & O'Neill, 2009), basaltic andesites (Hasenaka & Carmichael, 1987), lamprophyres (Carmichael, 1991), and magnetite and ilmenite series granites (Anderson, 1983).

5.2 Oxygen Fugacity Variations in the Halifax Pluton

Oxygen fugacity values obtained from samples on the margin and interior of the Halifax pluton reveal a distinction in redox state between these regions of the intrusion. As mentioned above, magmatic zircon from the interior of the Halifax pluton record ΔFMQ from -3.2 to 2.5, with an average of -0.2, whereas magmatic zircon from the margin yielded ΔFMQ values from -3.3 to 0.2, with an average of -1.2. This relative shift implies that the margin of the intrusion is somewhat more reduced than the interior.

39

One possible origin for the difference observed could be related to open system processes. The pluton shares a boundary with the Meguma Supergroup to the east, which in the field is observed as the juxtaposition of a biotite-monzogranite phase of the Halifax pluton and the graphitic slate and metasiltstone of the Cunard Formation (White & Goodwin, 2011). These rocks exhibit intense surficial weathering and oxidized surfaces, resulting from an abundance of pyrrhotite and pyrite (White & Goodwin, 2011).

Multiple lines of evidence suggest that the SMB has assimilated a significant amount of material from the Meguma terrane country rocks. Clarke & Carruzzo (2007) have identified xenocrystic, Meguma-derived ilmenite and rutile in the SMB. These xenocrysts are texturally and geochemically distinct from magmatic ilmenite and rutile of the SMB (Clarke & Carruzzo, 2007). The distribution of these xenocrysts is not homogenous across the batholith and seems to be concentrated in the least evolved intrusive phases (Clarke & Carruzzo, 2007), which in the case of the Halifax pluton, occurs along the margin. This relationship suggests a higher degree of contamination along the margins of the intrusion.

The abundance of pyrrhotite and pyrite within the Cunard Formation clearly provides potential to introduce sulfides into the SMB magma, and textural observations seem to confirm the presence of sulphides of external origin (Clarke et al, 2009). Clarke et al (2009) identified pyrrhotite, pyrite and chalcopyrite with a minor component of sphalerite, galena and arsenopyrite as inherited from the local country rocks. These inherited sulfides, like the inherited oxides, show both textural and geochemical evidence that ties them to the sediments of the Meguma terrane (Clarke et al, 2009). Furthermore, these sulfides are also concentrated along the marginal phases of the SMB. However, unlike the oxides, inherited sulfides are not present in any measurable abundances in the interior of the intrusion (Clarke et al, 2009). This serves as additional evidence that assimilation of the Meguma terrane was focused along the margins of the intrusion.

The assimilation of sulfide-rich, graphitic slates of the Cunard formation could be a significant factor when considering the perceived variation of fO_2 values from the margin to the interior of the Halifax pluton. The introduction of additional C, S and Fe to the SMB is noteworthy, as any of these elements has the potential to act as a reducing agent (Carmichael, 1991). Therefore, the process of assimilation of the Cunard formation has the potential to have had a reducing effect on the margins of the Halifax pluton.

Another possible origin for the observed difference in oxygen fugacity between interior and margin could be related to closed system processes. The following features suggest the marginal phase of the Halifax pluton is less differentiated than the interior. The marginal phase of the Halifax pluton has less SiO_2 and K_2O, and more Fe_2O_3, MgO, MnO and CaO than the interior. It also has less modal alkali feldspar, and more plagioclase and biotite. The abundance of biotite is important because ferromagnesian silicates can influence the redox state of a system (Carmichael, 1991). The early crystallisation of biotite can alter the prevailing redox state by removing ferrous iron from the system and increasing the Fe^{3+}/Fe^{2+}, which increases the relative oxygen fugacity (Carmichael, 1991). If the marginal phase of the Halifax pluton crystallised before the interior, and they are both derived from the same melt, the early crystallisation of biotite could have oxidized the system before the interior formed.

5.3 Oxygen Fugacity of Mineralised and Unmineralised Phases of the SMB

Although there is overlap to the values, unmineralised plutonic phases sampled in this study have an average ΔFMQ value of -0.31 and range from 2.51 to -3.33. The mineralised phase that hosts the Millet Brook deposit has an average ΔFMQ value of -2.08 and ranges from -0.46 to -3.76.

In addition to the fO_2, there are other differences between mineralised and unmineralised phases that are noteworthy. The mineralised sample contains the same rock forming minerals as the unmineralised (quartz, alkali feldspar, plagioclase and biotite), but is considerably coarser grained. Additionally, the mineralised sample contains the largest phenocrysts. The phases are also geochemically distinct, in that the mineralised sample has the highest Fe_2O_3, CaO and K_2O concentrations, which might reflect the phase's mineralogy. It also has the highest concentration of U, Zr and Y. Sample 18JC0021, which corresponds to the New Ross U deposit, was interpreted to be a monzogranite based on modal mineralogy observed in the field and in thin section. However, Chatterjee et al, (1982) states that the U deposits in the SMB are associated with the least differentiated phases of the SMB. If this is a more accurate representation of the whole suite, then perhaps its less evolved nature is related to the relatively lower fO_2, in a similar fashion than the difference between the margin and the interior of the Halifax pluton.

Chapter 6. Conclusions

6.1 Summary

      The Halifax, Sandy Lake and New Ross plutons were sampled to investigate the potential variation of oxygen fugacity within the South Mountain Batholith. Upon initial examination of trace element data and analysis of zircon CL-images, two distinct groupings of zircon became apparent. Based on the classification outlined in Yang et al, (2014), the zircons in the SMB can be classified into magmatic and non-magmatic, with a subdivision in the latter group between metamict and hydrothermal zircon. The Ce-in-zircon oxygen barometer was employed for analyses of magmatic zircon in order to investigate the record of fO_2. Measured oxygen fugacities show a variation of 4-5 orders of magnitude within the batholith, with differences also observed between mineralised and unmineralised samples, with the former being more reduced. Variations in oxygen fugacity also exists within a single pluton. Most notably, the Halifax pluton shows different fO_2 values in its margin and interior. This difference could be attributed to the process of assimilation, and the associated contamination from surrounding sulfide-rich, graphitic slates, or by internal magmatic differentiation involving biotite. Finally, although the SMB shows a large variation in fO_2 values, the intrusion is generally reduced, within the expected range for silicic magmas and specifically S-type granites.

6.2 Future Work

      There are 3 lines of work that seem particularly important based on the results of this study. First, and perhaps most importantly, the need to constrain the concentration of dissolved H_2O in the melt. This parameter imparts an important control on the redox state of the SMB and should therefore be constrained in more detail. A possibility would be to investigate fluid inclusions in both zircon and in heavy minerals that crystallize at similar pressure and temperature ranges to improve our understanding of how water behaved in the SMB melt. Additionally, a similar survey could be conducted with a different redox-sensitive system for comparison and perhaps a different range of conditions. Finally, it would be interesting to investigate in more detail the redox state of other mineralised intrusion of the SMB. This could help determine if the lower oxygen fugacity is unique to New Ross or a common feature in other mineralised phases of the SMB.

References

Anderson, J. L. (1983). Proterozoic anorogenic granite plutonism of North America. *Geological Society of America Memoir*, *161*, 133-154.

Baker, D. R., & Alletti, M. (2012). Fluid saturation and volatile partitioning between melts and hydrous fluids in crustal magmatic systems: The contribution of experimental measurements and solubility models. *Earth-Science Reviews*, *114*(3-4), 298-324.

Ballard, J. R., Palin, M. J., & Campbell, I. H. (2002). Relative oxidation states of magmas inferred from Ce (IV)/Ce (III) in zircon: application to porphyry copper deposits of northern Chile. *Contributions to Mineralogy and Petrology*, *144*(3), 347-364.

Blevin, P. L. (2004). Redox and compositional parameters for interpreting the granitoid metallogeny of eastern Australia: Implications for gold-rich ore systems. *Resource Geology*, *54*(3), 241-252.

Buddington, A. F., & Lindsley, D. H. (1964). Iron-titanium oxide minerals and synthetic equivalents. *Journal of petrology*, *5*(2), 310-357.

Carmichael, I. S. (1991). The redox states of basic and silicic magmas: a reflection of their source regions?. *Contributions to Mineralogy and Petrology*, *106*(2), 129-141.

Carmichael, I.S.E. & Ghiorso, M.S. (1990) Controls of Oxidation-Reduction Relations in Magmas. *Mineralogical Society of America: Review in Mineralogy, 24 (7),* 191-212.

Clarke, D. B. (1981). The mineralogy of peraluminous granites; a review. *The Canadian Mineralogist*, *19*(1), 3-17.

Clarke, D. B., & Carruzzo, S. (2007). Assimilation of country-rock ilmenite and rutile in the South Mountain Batholith, Nova Scotia, Canada. *The Canadian Mineralogist*, *45*(1), 31-42.

Clarke, D. B., Erdmann, S., Samson, H., & Jamieson, R. A. (2009). Contamination of the South Mountain Batholith by sulfides from the country rocks. *The Canadian Mineralogist*, *47*(5), 1159-1176.

Clarke, D. B., Grujic, D., McCuish, K. L., Sykes, J. C., & Tweedale, F. M. (2013). Ring schlieren: description and interpretation of field relations in the Halifax Pluton, South Mountain Batholith, Nova Scotia. *Journal of Structural Geology*, *51*, 193-205.

Chatterjee, A. K., Robertson, J., & Pollock, D. (1982). A summary on the petrometallogenesis of the uranium mineralization at Millet Brook, South Mountain Batholith, Nova Scotia. *Nova Scotia Department of Mines and Energy Report*, *82*(1), 57-67.

Eberz, G. W., Clarke, D. B., Chatterjee, A. K., & Giles, P. S. (1991). Chemical and isotopic composition of the lower crust beneath the Meguma Lithotectonic Zone, Nova Scotia: evidence from granulite facies xenoliths. *Contributions to Mineralogy and Petrology*, *109*(1), 69-88.

Ferry, J. M., & Watson, E. B. (2007). New thermodynamic models and revised calibrations for the Ti-in-zircon and Zr-in-rutile thermometers. Contributions to Mineralogy and Petrology, 154(4), 429-437.

Frost, B. R. (1991). Introduction to oxygen fugacity and its petrologic importance. *Reviews in Mineralogy and Geochemistry*, *25*(1), 1-9.

Holtz, F., Behrens, H., Dingwell, D. B., & Johannes, W. (1995). H2O solubility in haplogranitic melts: compositional, pressure, and temperature dependence. *American Mineralogist*, *80*(1-2), 94-108.

Hasenaka, T., & Carmichael, I. S. (1987). The cinder cones of Michoacan-Guanajuato, central Mexico: petrology and chemistry. *Journal of Petrology*, *28*(2), 241-269.

Hoskin, P. W., & Schaltegger, U. (2003). The composition of zircon and igneous and metamorphic petrogenesis. *Reviews in Mineralogy and Geochemistry, 53*.

Horne, R. J., MacDonald, M. A., Corey, M. C., & Ham, L. J. (1992). Structure and emplacement of the South Mountain batholith, southwestern Nova Scotia.

Keen, C. E., Kay, W. A., Keppie, D., Marillier, F., Pe-Piper, G., & Waldron, J. W. F. (1991). Deep seismic reflection data from the Bay of Fundy and Gulf of Maine: tectonic implications for the northern Appalachians. *Canadian Journal of Earth Sciences*, *28*(7), 1096-1111.

Kontak, D. J. (1990). The East Kemptville topaz-muscovite leucogranite, Nova Scotia; I, Geological setting and whole-rock geochemistry. *The Canadian Mineralogist*, *28*(4), 787-825.

Smythe, D. J., Brenan, J. M., Bennett, N. R., Regier, T., & Henderson, G. S. (2013). Quantitative determination of cerium oxidation states in alkali-aluminosilicate glasses using M4, 5-edge XANES. *Journal of Non-Crystalline Solids*, *378*, 258-264.

MacDonald, M. A. (2001). Geology of the South Mountain Batholith, Southwestern Nova Scotia. Nova Scotia Department of Natural Resources, Open File Report ME 2001-2.

Mallmann, G., & O'neill, H. S. C. (2009). The crystal/melt partitioning of V during mantle melting as a function of oxygen fugacity compared with some other elements (Al, P, Ca, Sc, Ti, Cr, Fe, Ga, Y, Zr and Nb). *Journal of Petrology*, *50*(9), 1765-1794.

Murphy, J. B., Hamilton, M. A., & LeBlanc, B. (2011). Tectonic significance of Late Ordovician silicic magmatism, Avalon terrane, northern Antigonish Highlands, Nova Scotia. *Canadian Journal of Earth Sciences*, *49*(1), 346-358.

Nasdala, L., Lengauer, C. L., Hanchar, J. M., Kronz, A., Wirth, R., Blanc, P., ... & Seydoux-Guillaume, A. M. (2002). Annealing radiation damage and the recovery of cathodoluminescence. *Chemical Geology*, *191*(1-3), 121-140.

Phillips, G. N., Wall, V. J., & Clemens, J. D. (1981). Petrology of the Strathbogie Batholith; a cordierite-bearing granite. *The Canadian Mineralogist*, *19*(1), 47-63.

Sasaki, A., & Ishihara, S. (1979). Sulfur isotopic composition of the magnetite-series and ilmenite-series granitoids in Japan. *Contributions to Mineralogy and Petrology*, *68*(2), 107-115.

Schenk, P. E. (1997). Sequence stratigraphy and proveance on Gondwana's margin: The Meguma Zone (Cambrian to Devonian) of Nova Scotia, Canada. *Geological Society of America Bulletin*, *109*(4), 395-409.

Shellnutt, J. G., & Dostal, J. (2015). Granodiorites of the South Mountain Batholith (Nova Scotia, Canada) derived by partial melting of Avalonia granulite rocks beneath the Meguma terrane: Implications for the heat source of the Late Devonian granites of the Northern Appalachians. *Tectonophysics*, *655*, 206-212.

Smythe, D. J., Brenan, J. M., Bennett, N. R., Regier, T., & Henderson, G. S. (2013). Quantitative determination of cerium oxidation states in alkali-aluminosilicate glasses using M4, 5-edge XANES. *Journal of Non-Crystalline Solids*, *378*, 258-264.

Smythe, D. J., & Brenan, J. M. (2016). Magmatic oxygen fugacity estimated using zircon-melt partitioning of cerium. *Earth and Planetary Science Letters*, *453*, 260-266.

Trail, D., Watson, E. B., & Tailby, N. D. (2012). Ce and Eu anomalies in zircon as proxies for the oxidation state of magmas. *Geochimica et Cosmochimica Acta*, *97*, 70-87.

White, C. E., & Goodwin, T. A. (2011). Lithogeochemistry, petrology, and the acid-generating potential of the Goldenville and Halifax groups and associated granitoid rocks in metropolitan Halifax Regional Municipality, Nova Scotia, Canada.

Yang, W. B., Niu, H. C., Shan, Q., Sun, W. D., Zhang, H., Li, N. B., ... & Yu, X. Y. (2014). Geochemistry of magmatic and hydrothermal zircon from the highly evolved Baerzhe alkaline granite: implications for Zr–REE–Nb mineralization. *Mineralium Deposita, 49*(4), 451-470.

Appendix A

Table 6. Zircon element concentrations (ppm) used for Ce-in-zircon oxygen barometer.

Analysis	Y	La	Ce	Pr	Nd	Sm	Eu	Gd	Tb	Dy	Ho	Er	Tm	Yb	Lu
18JC0003_1a	850	0	3	0	2	2	0	14	5	71	26	138	29	274	54
18JC0003_1b	1300	0	2	0	2	3	0	16	7	103	41	209	46	430	84
18JC0003_2a	840	Below LOD	1	0	1	5	0	32	10	98	26	98	17	138	24
18JC0003_2b	904	0	1	0	2	4	0	31	9	96	28	118	22	192	36
18JC0003_7a	1950	0	9	0	7	13	2	59	17	194	61	289	55	484	95
18JC0003_7b	1218	0	14	0	2	5	1	26	8	107	39	191	38	340	67
18JC0003_10a	683	0	23	0	1	3	1	15	5	58	21	109	23	228	47
18JC0003_10b	2180	0	1	0	1	3	0	22	11	166	65	343	74	723	132
18JC0003_14a	1880	4	21	3	26	20	2	65	18	191	63	278	51	438	80
18JC0003_14b	1676	2	13	2	13	13	2	49	14	156	55	254	47	403	75
18JC0003_18a	2140	0	29	0	2	6	1	34	13	178	62	329	69	644	126
18JC0003_18b	2770	3	16	3	21	11	1	42	16	218	87	458	103	1001	191
18JC0003_22a	6200	19	106	24	127	71	4	177	64	670	162	534	87	670	89
18JC0003_22b	4860	16	91	17	108	58	3	123	35	416	151	765	171	1720	328
18JC0003_24a	2194	4	22	4	25	16	1	39	13	170	67	379	93	1003	197
18JC0003_24b	2780	3	16	3	19	13	1	43	16	221	84	432	97	936	180
18JC0003_25a	1920	0	1	0	2	7	0	46	17	199	62	254	44	344	62
18JC0003_27a	2710	0	3	0	3	6	0	42	17	226	86	418	85	760	146
18JC0003_27b	1430	0	8	0	1	2	1	19	8	102	46	243	53	517	111
18JC0004_1a	3390	1	16	1	9	13	2	74	25	323	114	519	97	797	146
18JC0004_1b	4200	7	43	4	25	16	1	56	22	324	126	686	162	1610	316
18JC0004_2a	3510	5	50	7	46	43	2	120	33	371	120	518	99	825	151
18JC0004_2b	2377	1	10	1	8	10	0	40	15	204	76	384	84	783	155

Analysis	Y	La	Ce	Pr	Nd	Sm	Eu	Gd	Tb	Dy	Ho	Er	Tm	Yb	Lu
18JC0004_7a	1784	Below LOD	2	0	4	8	0	42	14	168	57	256	52	448	86
18JC0004-7b	1900	1	7	1	10	15	1	73	23	227	57	200	34	256	45
18JC0004_8a	2050	16	68	17	104	70	2	114	22	211	65	287	67	651	127
18JC0004_8b	3690	16	72	17	122	71	3	136	32	348	109	490	99	883	175
18JC0004_10a	1160	57	174	28	143	64	3	101	18	149	37	145	30	252	51
18JC0004_10b	1940	8	48	10	63	46	2	75	18	176	56	275	67	635	131
18JC0004_13a	1773	0	6	0	4	8	1	41	14	164	57	247	51	437	85
18JC0004_13b	3120	7	31	8	53	31	1	79	24	283	93	441	96	800	154
18JC0008_1a	3570	1	9	1	9	9	1	49	19	268	108	567	132	1204	250
18JC0008_1b	6060	7	34	7	44	32	5	99	35	469	186	988	240	2240	461
18JC0008_1c	2450	2	10	2	10	8	1	32	13	182	74	388	87	819	173
18JC0008_8a	1452	0	7	0	3	5	1	29	10	120	46	234	49	442	93
18JC0008_8b	1349	1	3	0	3	4	0	24	9	112	43	208	45	410	85
18JC0008_8c	3580	1	6	1	7	8	1	39	17	259	105	568	132	1284	254
18JC0008_9a	935	0	3	0	1	3	0	20	6	82	32	155	30	286	57
18JC0008_9b	2180	Below LOD	1	0	1	3	0	24	11	166	70	379	78	782	150
18JC0008_15a	2170	0	2	0	2	3	0	26	11	166	72	397	82	840	162
18JC0008_15b	2680	2	6	1	9	8	1	36	14	209	88	500	103	1084	206
18JC0008_16a	1170	54	127	20	74	25	3	44	10	105	35	181	38	439	91
18JC0008_16b	2110	0	3	0	3	5	0	35	13	185	72	381	70	710	130
18JC0008_16c	2570	0	1	0	1	3	0	29	13	198	86	466	91	961	178
18JC0008_18a	3280	0	8	0	7	12	2	69	23	294	112	556	102	1010	183
18JC0008_18b	1920	0	1	0	1	3	0	24	10	152	64	346	69	717	134
18JC0008_20a	867	0	7	0	2	3	0	14	5	71	30	156	30	311	59
18JC0008_20b	2890	1	5	1	4	5	0	32	15	222	98	561	117	1244	233
18JC0008_24a	1250	Below LOD	2	0	1	3	0	19	8	110	44	223	42	417	78
18JC0008_24b	2140	1	7	1	5	6	1	33	13	185	74	374	71	674	121
18JC0008_27a	7330	0	15	1	12	28	4	173	56	709	257	1193	212	1930	342
18JC0008_27b	2140	0	1	0	1	2	0	21	10	159	69	383	83	843	164

Analysis	Y	La	Ce	Pr	Nd	Sm	Eu	Gd	Tb	Dy	Ho	Er	Tm	Yb	Lu
18JC0010_1a	950	1	12	0	2	2	0	9	4	64	28	160	39	377	85
18JC0010_1b	2800	9	31	5	28	24	2	70	23	259	85	397	85	743	143
18JC0010_2a	1990	2	12	1	9	10	1	42	15	188	64	298	63	536	107
18JC0010_2b	4420	4	18	3	20	21	2	72	27	360	136	690	167	1610	333
18JC0010_9a	3810	7	33	6	39	38	3	87	28	293	96	471	117	1180	238
18JC0010_9b	3260	2	10	1	9	7	1	33	16	224	79	454	122	1300	290
18JC0010_10a	2380	1	13	1	6	9	1	48	17	212	76	350	71	581	115
18JC0010_10b	3040	2	10	2	12	12	1	45	17	240	93	490	117	1067	227
18JC0010_11a	3550	1	28	1	8	11	1	58	22	285	106	544	116	979	211
18JC0010_11b	2950	1	7	1	7	8	0	39	17	241	90	490	114	1000	217
18JC0010_14a	760	4	11	1	5	3	0	16	5	67	24	119	25	212	47
18JC0010_14b	4560	2	16	2	14	15	2	63	27	369	134	736	197	1940	417
18JC0010_15a	1740	0	3	0	2	5	0	33	12	149	53	266	54	456	99
18JC0010_15b	2950	2	8	1	6	6	0	35	15	221	86	466	107	940	197
18JC0010_16a	1400	1	4	1	6	9	0	40	12	146	48	223	43	345	71
18JC0010_16b	2730	2	10	2	13	13	1	49	18	233	83	438	90	784	162
18JC0010_18a	3110	Below LOD	1	0	1	4	0	42	18	234	89	451	98	836	183
18JC0010_18b	3580	0	2	0	1	3	0	33	16	259	109	623	150	1390	294
18JC0017_1a	3160	0	2	0	3	8	0	64	27	325	93	359	62	500	85
18JC0017_1b	5020	1	5	1	6	9	1	63	35	478	131	493	86	676	106
18JC0017_1c	2940	0	1	0	2	8	0	63	30	336	75	201	24	135	16
18JC0017_3a	1850	1	7	1	7	9	1	38	13	166	59	279	57	528	99
18JC0017_3b	5270	1	5	1	5	8	0	54	29	435	162	854	197	1960	345
18JC0017_3c	1530	2	11	2	13	13	1	47	13	142	48	219	42	370	70
18JC0017_6a	1880	Below LOD	2	0	2	6	0	35	13	169	62	305	63	572	108
18JC0017_6b	3000	5	36	7	48	48	4	105	30	304	88	408	89	913	169
18JC0017_7a	1830	0	3	0	2	6	1	37	13	162	59	285	58	520	100
18JC0017_7b	2290	1	6	1	5	6	1	32	13	186	70	361	78	721	138

Analysis	Y	La	Ce	Pr	Nd	Sm	Eu	Gd	Tb	Dy	Ho	Er	Tm	Yb	Lu
18JC0017_9a	1639	Below LOD	1	0	1	4	0	31	12	150	48	205	37	294	51
18JC0017_9b	1658	0	0	0	1	4	0	34	15	179	45	132	17	100	11
18JC0017_11a	2140	0	1	0	1	4	0	34	14	187	62	283	55	491	89
18JC0017_11b	2160	0	1	0	1	3	0	25	11	160	66	355	79	760	149
18JC0017_12a	2700	0	1	0	2	8	0	56	21	257	84	351	61	492	85
18JC0017_12b	1655	Below LOD	1	0	1	3	0	24	11	146	50	214	40	328	55
18JC0017_12c	2540	Below LOD	1	0	1	5	0	41	17	233	77	337	61	497	85
18JC0017_15a	890	0	15	0	2	4	1	22	6	81	28	138	29	270	54
18JC0017_15b	728	0	12	0	2	4	1	17	5	64	23	115	24	220	46
18JC0017_15c	641	0	13	0	1	3	1	14	4	56	21	102	21	203	42
18JC0017_17a	3850	2	16	4	22	23	2	77	29	352	114	524	106	970	176
18JC0017_17b	2430	1	5	1	7	8	1	40	15	208	76	382	78	704	134
18JC0017_18a	3400	2	9	2	14	15	1	55	21	295	109	570	133	1350	248
18JC0017_18b	6490	6	37	6	30	25	5	88	39	563	210	1168	295	3190	601
18JC0017_18c	2020	1	3	1	6	7	0	35	14	178	63	290	55	471	86
18JC0017_21a	2970	0	3	0	7	14	1	72	23	275	97	437	84	702	130
18JC0017_21b	3050	0	1	0	1	4	0	34	17	234	89	453	95	872	159
18JC0017_21c	1770	0	1	0	1	3	0	30	13	170	50	173	29	208	32
18JC0020_8a	1570	3	24	3	14	19	1	49	18	188	52	237	46	387	66
18JC0020_8b	5480	8	91	16	88	104	2	189	76	737	165	605	114	982	149
18JC0020_9a	2020	1	3	0	3	5	0	37	17	200	54	189	30	227	36
18JC0020_9b	2120	2	7	1	6	7	0	37	17	207	59	237	48	430	73
18JC0020_10a	2600	1	9	2	10	15	0	70	28	304	75	230	32	190	23
18JC0020_10b	1893	0	1	0	1	4	0	33	16	197	54	189	30	214	31
18JC0020_18a	3990	1	11	2	10	13	0	52	23	323	127	652	150	1500	276
18JC0020_18b	1450	0	1	0	1	4	0	29	12	145	43	166	29	226	39
18JC0020_19a	2140	0	19	0	5	9	1	50	17	204	74	329	64	560	99
18JC0020_19a1	930	2140	3200	269	820	118	1	77	15	119	25	76	12	85	13
18JC0020_19b	4850	0	1	0	1	6	0	67	35	469	126	415	58	363	44

Analysis	Y	La	Ce	Pr	Nd	Sm	Eu	Gd	Tb	Dy	Ho	Er	Tm	Yb	Lu
18JC0020_20a	840	0	23	0	2	4	1	21	7	83	24	97	17	136	24
18JC0020_20b	1324	Below LOD	0	0	1	3	0	26	12	139	39	139	22	162	25
18JC0020_22a	1521	0	8	1	4	7	1	20	10	128	47	255	63	678	149
18JC0020_22b	5550	0	2	0	2	8	0	75	41	528	147	504	82	593	84
18JC0020_26a	6090	10	105	17	101	108	2	214	82	784	167	543	89	685	95
18JC0020_26b	15520	62	723	110	647	652	14	1082	375	2930	480	1367	232	1798	221
18JC0020_27a	1075	0	20	0	6	9	2	38	10	108	34	153	29	263	50
18JC0020_27b	2103	0	1	0	1	4	0	39	18	212	58	206	32	229	34
18JC0021_1a	3810	0	3	0	7	15	1	91	30	358	123	558	107	915	170
18JC0021_1b	2090	0	1	0	2	6	0	41	15	189	66	300	56	475	86
18JC0021_4a	3290	1	4	1	7	17	1	87	26	307	104	473	90	801	149
18JC0021_4b	2440	0	4	0	4	9	1	56	19	238	84	389	75	637	118
18JC0021_9a	2590	0	1	0	1	4	0	38	16	223	79	374	75	683	129
18JC0021_9b	3180	0	1	0	3	9	0	65	25	316	105	458	83	670	116
18JC0021_10a	2550	8	3	2	11	9	1	53	19	239	80	355	66	561	101
18JC0021_10b	2740	111	28	27	124	36	6	74	22	258	82	360	67	590	107
18JC0021_16a	3480	4	30	3	21	22	3	89	28	336	115	534	103	900	164
18JC0021_16b	2160	0	3	0	1	3	0	22	11	165	65	334	73	687	130
18JC0021_18a	830	Below LOD	0	0	1	3	0	26	9	92	24	90	15	114	18
18JC0021_18b	1890	0	1	0	2	4	0	35	14	171	57	246	45	388	70
18JC0021_21a	4550	0	2	0	9	18	1	108	35	417	147	661	122	1060	186
18JC0021_21b	2410	6	23	5	30	26	6	75	26	276	77	311	57	472	80
18JC0021_25a	2060	1	5	1	5	8	0	44	16	190	65	301	56	482	86
18JC0021_25b	2290	0	2	0	2	6	0	42	16	205	73	335	64	556	101
18JC0021_29a	1930	0	2	0	2	6	0	43	14	183	63	288	55	479	88